



Eidgenössische Technische Hochschule Zürich
Swiss Federal Institute of Technology Zurich

Optoacoustic-based GECI Biosensors

An Imaging and Characterization Study

Master Thesis

Dept. of Information Technology and Electrical Engineering

ETH Zurich

submitted by

Xiyan Chen

chenxiy@student.ethz.ch

under the supervision of

Prof. Dr. Daniel Razansky

Co-supervisor: Xiang Liu

Zurich, August 2025

Contents

Abstract	1
Chapter 1: Introduction	2
1.1 Significance of brain imaging.....	2
1.2 Ideal spatial and temporal scales for brain imaging.....	3
1.3 Trade-offs of common current imaging modalities	4
1.4 Genetically Encoded Calcium Indicator (GECI): Design strategy	5
1.5 Fluorescence-based GECIs	7
1.6 Optoacoustic-based GECIs	10
1.7 Thesis: Design strategy and outline	12
1.8 Thesis: Future direction	13
Chapter 2: Materials and Methods	16
2.1 Confocal and optoacoustic imaging in HEK293-T cells	16
Cell culturing: HEK293-T cells	16
Preparation of GECI plasmids	17
Transfected GECI plasmids into HEK293-T cells.....	18
Incubation, medium change, and/or cell passaging until imaging	20
Introducing biliverdin, confocal, and OAM imaging.....	21
2.2 Confocal and optoacoustic imaging in <i>E. Coli</i>	25
Transformation.....	25
Imaging preparation	26
Confocal and OAM imaging.....	27
2.3 Protein purification	28
Transformation.....	28
Miniculture and Maxiculture	29
Harvest bacteria.....	30

Protein extraction from bacteria.....	31
Protein purification with column	32
2.4 Protein characterization	34
Protein concentration determination	35
Absorbance, excitation, and emission spectra determination	36
Optoacoustic spectra determination	37
Chapter 3: Results and Discussion	40
3.1 Confocal imaging in HEK293-T cells	40
Effects of directed evolution	40
Calcium reaction	40
3.2 Optoacoustic imaging in HEK293-T cells.....	44
Unexpected calcium response	44
3.3 Confocal and optoacoustic imaging in <i>E. Coli</i>	49
Confocal imaging: Calcium reaction	49
Optoacoustic imaging: Calcium reaction	52
3.4 Protein characterization	55
Visual comparison of absorbance	55
Absorbance spectra	55
Excitation and emission spectra	57
Optoacoustic spectra	59
Chapter 4: Conclusion	62
References	63
Acknowledgements	66

Abstract

Advancements in brain imaging techniques have substantially contributed to both neuroscience research and clinical diagnostics. Among them, genetically encoded calcium indicators (GECIs) have emerged as powerful tools for monitoring calcium dynamics in living cells. In previous work of lab members, GECIs were engineered to function via the optoacoustic effect by applying directed evolution to NIR-GECO3, which is an intensiometric fluorescent calcium indicator derived from biliverdin-binding fluorescent proteins (BV-FPs). After eight rounds of evolution aimed at improving absorbance, optoacoustic signal strength, and photostability, three promising variants (V5.2, V6.2, and V8.4) were selected for detailed characterization.

In this thesis, our results highlight that GECI variants retain the potential for further optimization to improve OA signal output and dynamic contrast. Among the three variants, V8.4 demonstrated superior performance, exhibiting the highest overall optoacoustic signal and the most pronounced calcium-induced change in optoacoustic amplitude, outperforming both V5.2 and V6.2. These trends were consistent across *in cellulo* imaging, spectral characterization, and protein-level comparisons, establishing V8.4 as the most promising candidate for future development. Additionally, experiments in *E. coli* also confirmed the presence of calcium-induced optoacoustic responses.

This study supports the feasibility of developing optoacoustic GECIs and provides a foundation for future improvements toward achieving reliable, high-contrast calcium imaging using the optoacoustic effect.

Chapter 1: Introduction

1.1 Significance of brain imaging

Advancements in rapid, volumetric, and non-invasive *in vivo* brain imaging have become essential not only for deepening our fundamental understanding of neuroscience, but also for driving the development of translational applications in medical and clinical practice. For example, high-resolution imaging modalities enable researchers to visualize the spatial distribution and interaction of different brain cell types, shedding light on complex neuroanatomical structures and synaptic organization [1]. Furthermore, real-time neural interactions and large-scale network dynamics across various cognitive states can now be investigated through dynamic neuroimaging techniques such as Magnetoencephalography (MEG) and electroencephalography (EEG) [2]. By providing insights into neural connectivity and activity patterns, these imaging advances contribute significantly to building more accurate models of brain function and facilitate systems-level understanding of how distributed brain regions cooperate during behavior and cognition.

In addition to advancing basic neuroscience knowledge, *in vivo* brain imaging plays a crucial role in translational applications that bridge laboratory research and clinical practice. For instance, neuroimaging has become central to the diagnosis and monitoring of neurological disorders, with PET imaging widely used to detect abnormal brain metabolism and pathophysiological changes in diseases such as Alzheimer's and Parkinson's diseases [3]. Also, imaging critical biomarkers for therapeutic assessment provides unique insights into disease assessment and treatment. For example, *in vivo* imaging of amyloid- β deposits in the brains of living mice enables direct visualization of plaque clearance following immunotherapy treatment [4]. Moreover, reporter gene imaging enables the *in vivo* tracking of immune cell therapies in brain tumors, offering real-time evaluation of treatment efficacy [5]. Beyond disease-focused research, neuroimaging has also contributed to emerging technologies such as brain-computer interfaces (BCI), where imaging-guided approaches are used to decode neural

signals for controlling external devices, with applications ranging from rehabilitation to assistive communication [6]. Together, these translational advances highlight the critical importance of *in vivo* brain imaging across a broad spectrum of biomedical and clinical fields.

1.2 Ideal spatial and temporal scales for brain imaging

However, tremendous efforts still need to be put into achieving fast, high-resolution, high-sensitivity imaging at the multi-spatial and temporal levels. On the one hand, in terms of multi-spatial imaging, while significant progress has been made in imaging at both microscopic and macroscopic levels, we are still far from achieving an integrated understanding that connects molecular and cellular changes—such as gene expression patterns, regulatory events, and signaling pathway dynamics—with the large-scale tissue and organ-level alterations that eventually manifest as clinical disease symptoms [7]. Imaging at small spatial scales is particularly critical because many pathological processes are initiated at the molecular and cellular level long before any observable changes appear in tissue structure or organ function. Therefore, the ability to detect these early molecular alterations through high-resolution imaging techniques plays a pivotal role in early diagnosis, intervention, and a deeper mechanistic understanding of disease progression.

On the other hand, long-term *in vivo* brain imaging is equally essential. Neurodegenerative conditions such as Alzheimer's and Parkinson's disease typically develop over decades, with pathological changes accumulating gradually before clinical symptoms become evident [8]. Prolonged imaging over extended periods allows researchers to monitor disease progression dynamically, revealing how molecular and structural alterations evolve over time. This temporal perspective is critical for understanding disease mechanisms, identifying potential therapeutic windows, and evaluating the long-term efficacy of treatment strategies. Without longitudinal imaging data, our ability to connect early pathological events with later-stage clinical outcomes remains limited.

1.3 Trade-offs of common current imaging modalities

As shown in **Figure 1**, despite substantial progress in the field, current imaging technologies, including positron-emission tomography (PET), computerized tomography (CT), magnetic resonance imaging (MRI), and ultrasound, still face inherent trade-offs among spatial resolution, temporal resolution, sensitivity, imaging speed, and field of view [8]. For example, MRI brain imaging works by aligning hydrogen protons in the brain using a strong magnetic field. Radiofrequency pulses are applied to disrupt this alignment, and as the protons return to their original state, the emitted signals are detected, processed, and used to create detailed images of the brain's structure based on differences in tissue properties. MRI allows for non-invasive, whole-brain imaging with anatomical contrast. However, this method also suffers from limited cellular and sub-cellular sensitivity [8]. In contrast, PET works by detecting radiation emitted from a small amount of radioactive material injected into the body. The radioactive tracer emits positrons, which collide with electrons, producing gamma rays. These gamma rays are detected by the PET scanner and used to create detailed images, providing insights into metabolic activity and physiological functions at the cellular level. In general, current PET technology has high sensitivity, detecting very small changes in brain activity and the presence of biomarkers, but at the cost of lower spatial resolution than MRI and CT, which can affect the precision of anatomical details [3]. Also, it requires the application of an external radioactive source, which introduces procedural invasiveness and potential biological effects of the radiopharmaceutical while provides only limited observation window.

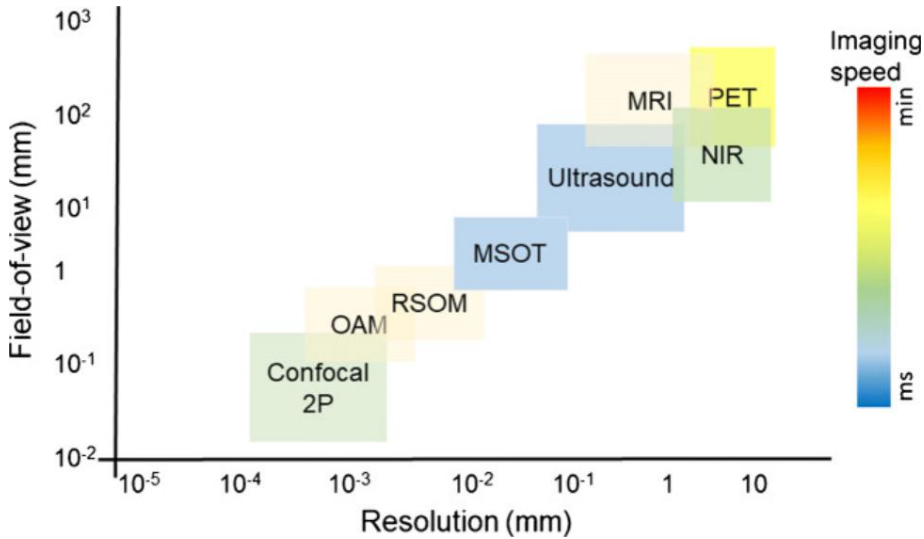


Figure 1: Comparison of various biomedical imaging modalities in terms of spatial resolution (x-axis) and field-of-view (y-axis), plotted on logarithmic scales. Each colored block represents the operational range of a modality: Confocal and two-photon microscopy (2P), optoacoustic microscopy (OAM), raster-scan optoacoustic mesoscopy (RSOM), multispectral optoacoustic tomography (MSOT), ultrasound, magnetic resonance imaging (MRI), positron emission tomography (PET), and near-infrared imaging (NIR). Imaging speed is indicated by the color gradient, with blue representing fast (millisecond-scale) imaging and red indicating slow (minute-scale) imaging. This visualization highlights the trade-offs between resolution, imaging depth, field-of-view, and acquisition speed among imaging techniques. Taken from Ref. [8].

1.4 Genetically Encoded Calcium Indicator (GECI): Design strategy

Molecular imaging using functionalized imaging agents is actively being explored as a promising approach for neural imaging, demonstrating strong potential for achieving high-performance and high-specificity outcomes. Among these agents, Genetically Encoded Calcium Indicators (GECIs) have emerged as a powerful tool due to their ability to report intracellular calcium dynamics in real time with cell-type specificity and minimal invasiveness.

GECIs typically consist of two functional components:

1. A calcium-sensing domain, which binds calcium ions (Ca^{2+}), and
2. A reporter domain, which translates calcium binding into a signal.

As illustrated in **Figure 2**, the design of NIR-GECO1 serves as a representative example. The calcium-sensing module is composed of calmodulin (CaM) and a CaM-binding peptide (RS20). Calmodulin is a ubiquitous calcium-binding messenger protein expressed in all eukaryotic cells. Upon binding calcium ions, calmodulin undergoes a conformational change that enables it to interact with target peptides such as RS20, thereby acting as both a calcium

sensor and a signal transducer. In this system, CaM and RS20 form a calcium-dependent interaction that modulates the structure of the adjacent reporter domain [9].

The reporter domain used in NIR-GECO1 is monomeric infrared fluorescent protein (mIFP), which belongs to the class of biliverdin-binding fluorescent proteins (BV-FPs). These proteins fluoresce in the far-red to near-infrared (NIR) spectrum when bound to biliverdin, a chromophore derived from heme catabolism. mIFP was chosen due to its deep tissue penetration and low background autofluorescence in biological tissues, making it suitable for *in vivo* imaging applications [9].

In this design, calcium binding causes a conformational change in the CaM-RS20 domain, which allosterically affects the environment of the chromophore in mIFP, thereby modulating its fluorescence. Notably, the fluorescence intensity exhibits an inverse correlation with calcium concentration: fluorescence is brighter at low calcium levels and becomes dimmer as calcium concentration increases. This reversible fluorescence response enables dynamic tracking of calcium fluctuations within live cells and tissues.

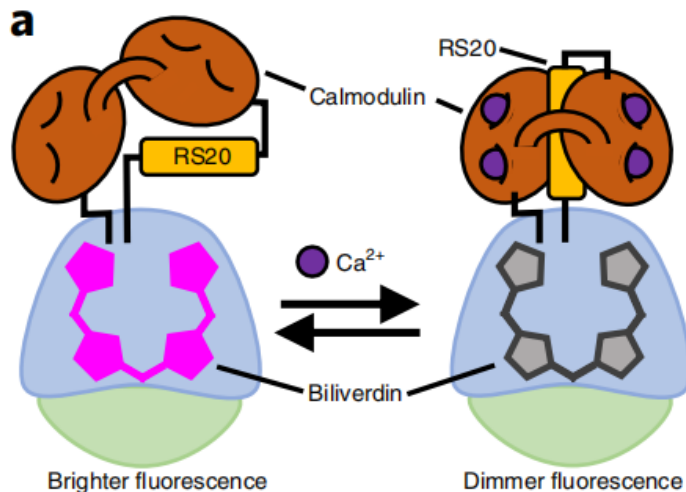


Figure 2: Schematic illustration of the molecular design and calcium-sensing mechanism of NIR-GECO1. The genetically encoded calcium indicator consists of a calcium-binding domain (Calmodulin-RS20) and a reporter domain (mIFP), a biliverdin-binding near-infrared fluorescent protein (BV-FP). In the absence of calcium (left), mIFP adopts a conformation that promotes higher fluorescence intensity. Upon calcium binding (right), Calmodulin interacts with RS20, inducing a conformational change that alters the local environment of the biliverdin chromophore, resulting in reduced fluorescence. Taken from Ref. [9].

In the context of GECIs, the reporter protein domain can be broadly categorized into two main types based on the nature of the emitted signal: (1) fluorescence-based GECIs and (2) optoacoustic-based GECIs. Below is a detailed explanation of each category, with further subdivisions based on the properties of the emitted light.

1.5 Fluorescence-based GECIs

Fluorescent proteins are one of the most commonly used types of reporters in GECIs. These proteins have significantly advanced optical imaging techniques and are now widely used in the study of various biological processes. In the context of GECIs, fluorescent proteins emit light upon excitation by an external light source, and the intensity of the emitted light correlates with changes in calcium concentration within cells. As reporter molecules, fluorescent proteins offer real-time, non-invasive imaging of calcium dynamics in living cells. Fluorescent proteins used in GECIs can be further classified into two subtypes based on the wavelength of the emitted light: visible fluorescent proteins and near-infrared (NIR) fluorescent proteins.

Visible fluorescent proteins

This subtype consists of β -barrel fluorescent proteins, which are homologs of the *Aequorea* green fluorescent protein (GFP). Many engineered and optimized fluorescent proteins used for GECIs operate within the visible wavelength range (~450–670 nm). Notable examples include green fluorescent protein (GFP)-based GECIs, such as the "GCaMP" series [10-12], and red fluorescent protein (RFP)-based GECIs, such as the "RCaMP" series [13, 14]. These visible fluorescent proteins are typically optimized for key performance metrics such as brightness, calcium ion affinity, signal-to-noise ratio, and cooperativity [10, 14, 15]. However, these visible fluorescent proteins present several challenges. The short wavelengths of visible light lead to strong spectral overlap with other indicators and optogenetic actuators, as well as high phototoxicity, autofluorescence, and intense light scattering in tissues. These factors limit tissue penetration, reduce optical resolution, and ultimately result in shallow imaging depth [9, 15].

Near-infrared (NIR) fluorescent proteins

The second type of fluorescent proteins: far-red to near-infrared (NIR) fluorescent biliverdin-binding proteins (BV-FPs), are derived from bacteriophytochromes (BphPs) or other biliverdin-binding proteins. The structure of biliverdin and the heme metabolism pathway is shown in **Figure 3**. Biliverdin is a crucial intermediate in the metabolism of heme, a tetrapyrrole compound that plays a central role in oxygen transport. Biliverdin is generated when heme undergoes oxidation by the enzyme heme oxygenase, which cleaves the heme molecule, releasing carbon monoxide and producing biliverdin. This intermediate is then converted into bilirubin by the action of the enzyme biliverdin reductase. Biliverdin itself possesses antioxidant properties, helping to protect cells from oxidative damage by scavenging free radicals [16].

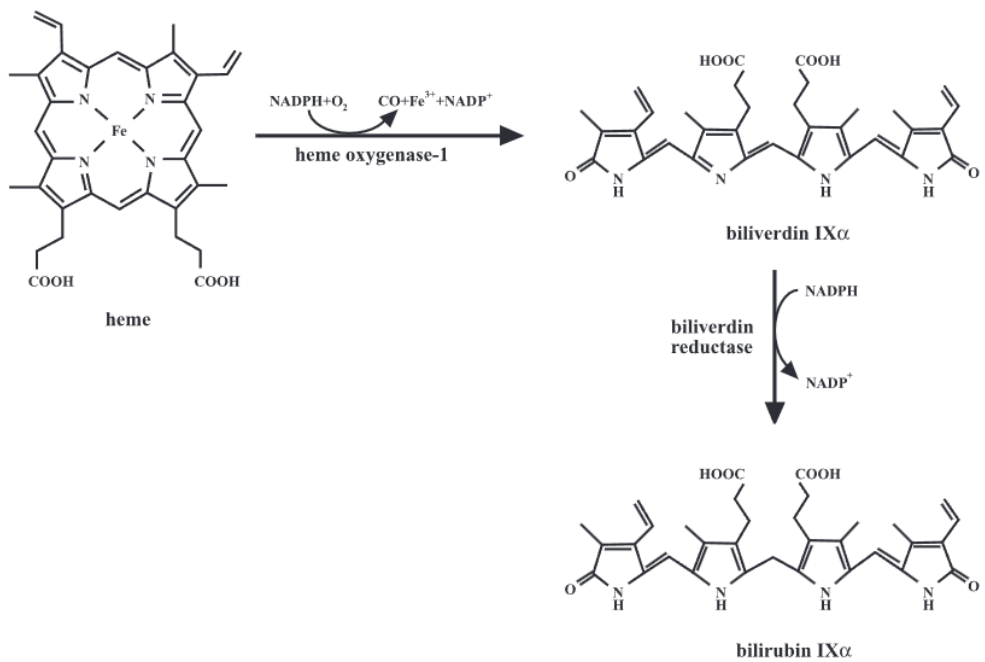


Figure 3: Schematic representation of the heme metabolism pathway. Heme is converted into biliverdin by the enzyme heme oxygenase, which catalyzes the oxidative cleavage of heme. Biliverdin is subsequently reduced to bilirubin by the enzyme biliverdin reductase. This pathway plays a critical role in the breakdown of heme and the regulation of bilirubin levels in the body. Taken from Ref. [16].

BphPs rely on the biliverdin as a chromophore, which absorbs light in the NIR region and exhibits fluorescence emission, which is ubiquitous in most eukaryotic organisms [17]. The overall structure of the photosensory module of BphPs is shown in **Figure 4**. The BphP photosensory module is composed of two or three protein domains connected by α -helices,

including PAS, GAF, and PHY domains. It can exist in different forms, including monomers, dimers, or oligomers and generally monomers are preferable. The chromophore biliverdin is positioned within a pocket of the GAF domain, where it is covalently attached to a cysteine (Cys) residue in the PAS domain. When BV absorbs light, it undergoes a conformational change that is sensed by the photosensory module. This change is then relayed to the effector domain, triggering the light-induced molecular signaling pathway [17].

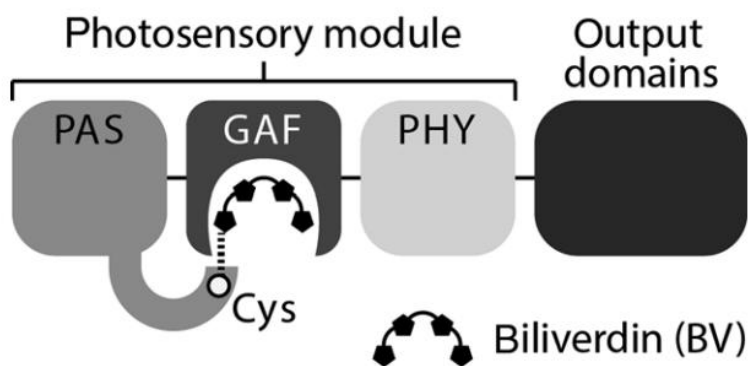


Figure 4: Schematic representation of the photosensory module in a bacteriophytochrome-based system. The module consists of three domains: PAS, GAF, and PHY. The PAS domain contains a cysteine (Cys) residue that covalently binds to the chromophore biliverdin, which undergoes a conformational change upon light absorption. This photosensory module is connected to output domains, which transmit the light-induced signal, triggering downstream molecular responses. The binding of biliverdin to the protein structure plays a crucial role in modulating the protein's function in response to light. Taken from Ref. [17].

For GECI, to overcome the challenges mentioned with β -barrel fluorescent proteins, significant efforts have also been made to engineer fluorescent proteins that operate in the NIR range (~670–720 nm), which offers more favorable spectral properties for deep-tissue imaging and exploits the optical window where endogenous chromophores have low absorption. Despite advancements, NIR-GECIs are still in their developmental stages and require further optimization to achieve performance levels comparable to visible wavelength GECIs [15]. For example, NIR-GECO1 shown in **Figure 2**, an intensiometric biliverdin-binding GECI, has shown low efficiency and limited contrast for *in vivo* imaging [9]. The later-evolved versions of NIR-GECO1, designated NIR-GECO2 and NIR-GECO2G, have improved upon certain aspects but still face challenges, such as reduced brightness, slower response kinetics, and

susceptibility to photobleaching when compared to the latest green and red fluorescent GECIs [15].

1.6 Optoacoustic-based GECIs

Optoacoustic imaging, also known as photoacoustic imaging, is based on the optoacoustic effect, a physical phenomenon in which acoustic (ultrasound) waves are generated as a result of light absorption by optical absorbers, as shown in **Figure 5** below. When short laser pulses in the nanosecond range irradiate tissue or biological samples, chromophores such as hemoglobin, melanin, or engineered fluorescent proteins absorb the light energy. This rapid absorption leads to a transient temperature rise, which causes thermoelastic expansion of the surrounding medium. Due to the ultrashort timescale and the localized nature of the heating, this expansion occurs under adiabatic conditions, generating broadband ultrasound waves. These ultrasound waves propagate through the tissue and are subsequently detected by an ultrasonic transducer. The transducer converts the acoustic pressure signals into electrical signals, which are then digitized and processed to reconstruct spatial images [18-20].

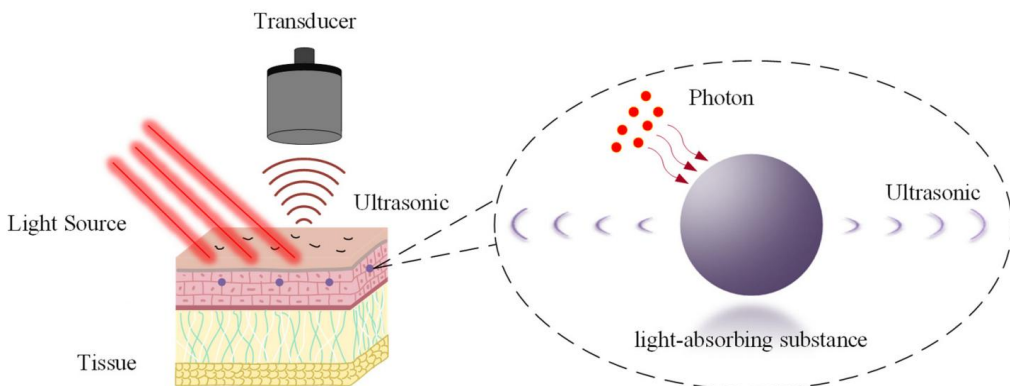


Figure 5: Principle of optoacoustic imaging. When pulsed laser light irradiates tissue, light-absorbing substances (e.g., chromoproteins or endogenous absorbers) absorb the photons and undergo thermoelastic expansion, generating ultrasonic waves. These ultrasound signals are then detected by a transducer to reconstruct images with high spatial resolution. This hybrid approach combines the molecular sensitivity of optical imaging with the deep penetration and spatial resolution of ultrasound. Taken from Ref. [21].

Optoacoustic imaging offers several distinct advantages that enable it to overcome the limitations faced by conventional optical imaging modalities. Most importantly, it combines the inherent strengths of both optics and ultrasound: on one hand, optics provides rich and

versatile optical absorption contrast that allows for molecular specificity; on the other hand, ultrasound offers excellent tissue penetration and spatial resolution due to its low scattering in biological media [22]. By converting absorbed optical energy into ultrasound waves, optoacoustic imaging bypasses the strong scattering that typically limits the depth of purely optical techniques such as fluorescence microscopy. As a result, optoacoustic can achieve imaging depths of several millimeters to centimeters while preserving high spatial resolution [23, 24]. Furthermore, because optoacoustic imaging relies on nanosecond pulsed excitation and can achieve high imaging frame rate, it enables real-time imaging with high temporal resolution, making it well-suited for monitoring dynamic biological processes, such as calcium signaling or hemodynamic changes [24-26]. In summary, optoacoustic imaging uniquely integrates optical contrast with acoustic penetration, providing a powerful platform for deep-tissue, high-resolution, and label-specific imaging—particularly beneficial in neuroscience, oncology, and vascular biology.

In terms of the optoacoustic-based GECI's reporter domain, non-fluorescent (or weakly fluorescent) chromoproteins are a subset of fluorescent proteins that are promising molecules. In contrast to fluorescent proteins that convert light to light, chromoproteins are usually optimized to increase the optical absorption and to decrease the quantum yield so that more energy is converted to acoustic signals to achieve the highest signal-to-noise ratio. Chromoproteins have been shown to be promising optoacoustic reporter molecules. For example, in 2012, a near-infrared fluorescent probe engineered from a bacteriophytochrome that binds biliverdin was successfully used for optoacoustic imaging *in vivo* [27]. Additionally, in 2016, dark chromoproteins were engineered via directed evolution to improve the signal-to-noise ratio for optoacoustic microscopy and fluorescence resonance energy transfer (FRET) imaging [28]. However, current GECIs based on chromoproteins still exhibit suboptimal performance. Specifically, they often suffer from insufficient photostability, where undesired residual fluorescence dominates over the optoacoustic signal. In addition, their relatively low molar extinction coefficients limit light absorption, resulting in weak acoustic signal generation.

Most critically, the change in signal upon calcium binding remains minimal, reducing their effectiveness as dynamic calcium sensors in optoacoustic imaging.

1.7 Thesis: Design strategy and outline

To develop and improve GECIs based on the optoacoustic effect, directed evolution was performed on NIR-GECO3, a genetically encoded near-infrared fluorescent calcium ion indicator derived from NIR-GECO1. NIR-GECO3 belongs to the family of near-infrared (NIR) biliverdin-binding fluorescent proteins (BV-FPs), and its fluorescence intensity exhibits an inverse correlation with intracellular calcium concentration. Since BV-FPs require biliverdin as a cofactor to fluoresce, the presence of biliverdin is essential for the function of NIR-GECO3 [9].

In previous work of the author and other lab members, eight rounds of directed evolution were carried out on NIR-GECO3 with the goal of enhancing absorbance, optoacoustic signal strength and calcium responsiveness, and photostability. From this process, three promising and representative protein variants were identified: V5.2, V6.2, and V8.4. In the naming convention, the number before the decimal point represents the round of directed evolution, and the number after the decimal point indicates the specific variant selected from that round. These variants were cloned into either the pDuEx2 or pRSET plasmid backbones.

However, since the obtained GECI plasmids were constructed in the pDuEx2 or pRSET backbone, their application was primarily limited to certain cell types. Therefore, to facilitate transfection in neural cells and enable potential future *in vivo* applications, switching to a pAAV backbone was necessary. The pAAV system offers advantages such as enhanced compatibility with mammalian expression systems, improved gene delivery efficiency, and better adaptability for downstream applications involving neural cell cultures and *in vivo* studies [29].

Also, as directed evolution was conducted in *Escherichia coli* (*E. coli*), and the codon adaptation index (CAI) for GECI proteins in mammalian cells was only approximately 0.75, codon optimization was necessary to enhance protein expression in mammalian systems. Therefore, codon optimization was performed for all four variants based on the sequence

provided in the plasmid map. Finally, the pAAV backbone was used to incorporate subsequent ligation with the obtained codon-optimized fragment and new GECI plasmids were prepared.

In this study, the codon-optimized GECI sequence, cloned into the pAAV backbone, was utilized to transfect mammalian HEK293-T cells for evaluating protein expression and calcium sensitivity *in cellulo*. Post-transfection, cells were subjected to both confocal fluorescence microscopy and optoacoustic microscope to assess overall expression, effects of directed evolution, and responsiveness to calcium fluctuations. The primary objective was to determine whether the sensor exhibits the expected inverse correlation between fluorescence intensity and intracellular calcium levels, and to investigate whether a reliable optoacoustic signal could be captured across different calcium conditions.

In parallel, the original GECI plasmids carried in the pRSET bacterial expression backbone were transformed into *E. coli* to explore sensor performance in a prokaryotic system. These experiments also provided complementary insights into the calcium-induced spectral changes in both fluorescence and optoacoustic domains.

In addition, purified GECI protein variants were systematically characterized *in vitro*. Spectral analysis was conducted to measure fluorescence and optoacoustic properties, and calcium titration experiments were performed to assess each variant's sensitivity and response dynamics. Together, these two complementary experimental approaches—cell-based imaging and biochemical characterization—provided a comprehensive evaluation of the performance and potential of the evolved GECI variants.

1.8 Thesis: Future direction

Further optimization of protein domains

In the present work, directed evolution efforts were focused exclusively on the reporter domain, which converts calcium binding into an optical and optoacoustic signal. While this approach successfully enhanced fluorescence and improved optoacoustic output, further refinement is possible. Specifically, the reporter domain could be engineered to have stronger optical absorption in the desired wavelength range, thereby boosting the optoacoustic signal

amplitude. In parallel, the calcium-sensing domain, which binds Ca^{2+} , represents another promising target for optimization. By increasing its calcium-binding affinity and tuning its dynamic range, the sensor could detect more subtle and rapid calcium fluctuations, enabling the monitoring of finer-scale neuronal signaling events. Incorporating rational design with high-throughput screening may accelerate these improvements.

***In vivo* characterization**

Since the ultimate goal of this optoacoustic-based GECI is to function in neurons within the intact brain, an essential next step is to evaluate its performance in living animals. Such *in vivo* characterization will allow assessment of the sensor's efficacy under realistic physiological conditions, including tissue scattering, absorption, and motion artifacts. In particular, longitudinal imaging in animal models could reveal the sensor's stability over time, its response to natural or evoked neuronal activity, and its compatibility with chronic implantation setups. This stage will also help to establish baseline parameters such as signal-to-noise ratio, detection depth, and spatial resolution in complex biological environments.

Comparison with other imaging modalities

For this optoacoustic-based GECI to be impactful, it must offer clear advantages over existing imaging modalities. Therefore, systematic benchmarking against established approaches is necessary. This comparison should consider not only sensitivity and temporal resolution but also penetration depth, photostability, and the ability to operate in scattering tissue. Mapping out the trade-offs between optoacoustic and purely optical methods will clarify the unique niches where this technology excels, such as deep-tissue, large-scale neuronal population imaging, or simultaneous functional and structural measurements.

Multimodal integration

Beyond improving standalone performance, integrating optoacoustic-based GECIs with complementary imaging modalities could substantially broaden their application scope. For instance, combining optoacoustic imaging with high-resolution fluorescence microscopy could enable dual-modality calcium measurements, providing both deep-tissue functional data and fine structural information. Similarly, coupling optoacoustic signals with magnetic resonance

imaging (MRI) could facilitate large-scale brain mapping by adding functional calcium readouts to anatomical MRI datasets. Multimodal strategies may also allow cross-validation of signals, reducing ambiguity and improving quantification. Such integration could position optoacoustic GECIs as a versatile component within the broader neuroimaging toolbox, capable of bridging scales from subcellular to whole-brain levels.

Chapter 2: Materials and Methods

2.1 Confocal and optoacoustic imaging in HEK293-T cells

A total of 13 transfection and subsequent confocal and optoacoustic imaging experiments were performed in HEK293-T cells to determine the optimal conditions for achieving the most efficient expression and strongest signal of the GECI sensor. Each transfection and imaging experiment took approximately one week, following a standardized procedure as illustrated in **Figure 6**. In brief, cells were first cultured, and once they reached approximately 80% confluence, GECI plasmids were transfected into the cells, with different transfection reagents being tested. Subsequently, various experimental conditions, such as incubation duration, medium change timing, and/or cell passaging, were explored to determine the best combination for maintaining optimal cell health on the day of imaging, both for confocal and optoacoustic imaging.

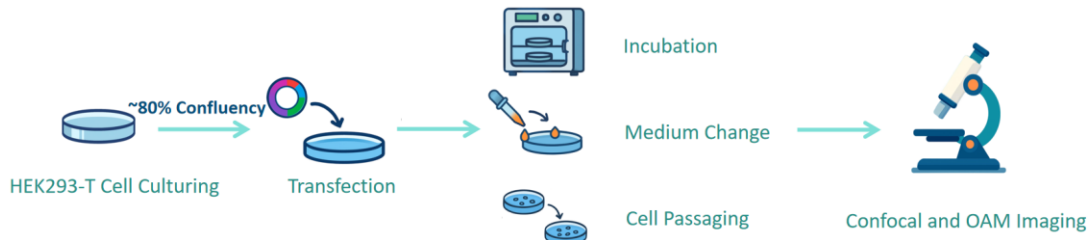


Figure 6: Workflow for transfection and subsequent imaging of HEK293-T cells. Cells are first cultured to approximately 80% confluence. Upon reaching this density, GECI plasmids are transfected into the cells using various transfection reagents. Subsequently, various experimental workflows, including incubation time, timing of medium change, and/or cell passaging, were tested to identify the optimal combination for ensuring the best cell health on the day of imaging. The cells are then analyzed using confocal and optoacoustic microscopy to assess protein expression and calcium sensitivity.

Cell culturing: HEK293-T cells

HEK293-T cells were cultured and maintained in Dulbecco's Modified Eagle Medium (DMEM), supplemented with 10% fetal bovine serum (FBS) (Thermo Fisher) to support cell growth and viability. The cells were passaged every three to four days, typically when they reached approximately 80% confluence, as assessed visually under the microscope. The average doubling time for HEK293-T cells was approximately 18 hours. The growth rate of the

cells was highest around passage 8 (P8), with a noticeable deceleration in growth observed after passage 13 (P13). For the transfection experiments, cells were generally selected from passages between P5 and P12. This range was chosen because the cells were actively proliferating, ensuring optimal cell health and receptivity for transfection.

Under an optical microscope, HEK293-T cells exhibit a characteristic epithelial-like morphology, appearing as flat, polygonal, and adherent cells with clear and well-defined edges. Each cell contains a prominent, round or oval nucleus, which is easily distinguishable. The cells grow in a monolayer, and as they reach higher confluence, they exhibit a cobblestone-like arrangement, with cells tightly packed together. At lower cell densities, the cells are well-separated with visible intercellular spaces between them. However, as confluence increases, the cells become more compact, with minimal gaps observed between neighboring cells. This characteristic arrangement reflects the dynamic nature of HEK293-T cell growth and their ability to form tight cell junctions at higher densities.

Preparation of GECI plasmids

The correctly ligated plasmids obtained from previous Miniprep were selected for amplification for each protein variant. The Maxiprep procedure followed the NucleoBond® PC 500 Maxi/BAC protocol for low-copy plasmid purification. However, slight modifications were made to the final precipitation and washing steps.

After elution and before precipitation, 10 μ l of the eluted DNA was collected to measure its concentration, allowing for the determination of the final volume of water needed to achieve a target DNA concentration of approximately 1 μ g/ μ l for efficient transfection. Following precipitation and DNA pellet formation, the pellet was transferred to a 1.5 mL tube using a pipette tip and centrifuged at 13,000 \times g for 5 minutes. The supernatant containing isopropanol was carefully removed using pipette tips to eliminate as much residual solvent as possible. Next, 0.5 mL of 70% ethanol was added to wash the DNA, followed by centrifugation at 13,000 \times g for another 5 minutes. The ethanol was then carefully removed using pipette tips, and the DNA pellet was left to air dry with the tube lid open to allow complete evaporation of residual ethanol.

Once dried, the appropriate volume of water was added to resuspend the DNA, ensuring a final concentration of approximately $1 \mu\text{g}/\mu\text{l}$ for downstream transfection experiments. All the GECI sequences in plasmids prepared by Maxiprep are later confirmed by DNA sequencing.

Transfected GECI plasmids into HEK293-T cells

When HEK cells reached approximately 80% confluence, they were collected and seeded into small dishes (9.6 cm^2 per dish). The volume of the cell suspension added to each dish was calculated to ensure that the cells would reach approximately 80% confluence the following day, just before transfection. This confluence was selected to optimize the transfection efficiency and ensure maximum cell viability. Approximately 20 hours later, the cells were transfected using the prepared plasmids, following the standard transfection protocol. To determine the most efficient transfection reagent, three different reagents were tested, allowing for a comparative evaluation of their effectiveness in terms of transfection efficiency, cell viability, and overall protein expression.

LipofectamineTM 3000 Reagent (Thermo Fisher)

The transfection procedure followed the protocol provided by Thermo Fisher. Tube A and Tube B were prepared using the reagents and materials listed in Table 1. For the initial transfection experiments, pure DMEM (without FBS) was used; however, it was later replaced with Opti-MEMTM I Reduced Serum Medium (Thermo Fisher) for improved transfection efficiency. Opti-MEM is preferred over DMEM because it is specifically optimized for transfection applications. This medium contains essential supplements such as insulin and transferrin, which help support cell viability under reduced-serum conditions. The formulation of Opti-MEM enhances the formation of stable DNA-lipid complexes and minimizes cytotoxicity, thereby improving overall transfection efficiency. After preparing Tube A and Tube B, the contents were mixed and incubated for 20 minutes at room temperature to allow stable DNA-lipid complex formation. Meanwhile, the medium in the culture dishes was replaced with 2 mL of pure DMEM. Once the DNA-lipid complexes had formed, the mixture from Tube A and Tube B was added to the cells, which were then gently mixed to ensure even distribution.

Table 1: Reagents and materials used for Lipofectamine™ 3000 Reagent transfection

Tube A	Tube B
125 μ l DMEM/Opti-MEM	125 μ l DMEM/Opti-MEM
7.5 μ l Lipofectamine 3000 Reagent	5 μ l P3000 Reagent
/	Plasmid DNA 2.5 μ g

TransIT-2020 (Mirus Bio) and Trans-LT1 (Mirus Bio)

Both TransIT-2020 and TransIT-LT1 reagents were tested for their transfection efficiency in HEK cells, and both reagents demonstrated good performance. No significant differences in transfection efficiency or toxicity were observed between the two. Moreover, upon visual inspection, it was evident that transfection with TransIT-2020 and TransIT-LT1 resulted in noticeably higher protein expression and lower cellular toxicity compared to Lipofectamine 3000. Specifically, 24 hours after transfection, the cells transfected with TransIT reagents appeared healthier, being able to maintain the epithelial-like morphology, whereas cells transfected with Lipofectamine 3000 appeared rounder and less healthy. This suggests that TransIT reagents may cause less cellular stress and maintain better cell viability. Additionally, the fluorescence signal in cells transfected with TransIT reagents was stronger compared to those transfected with Lipofectamine 3000, indicating more efficient transfection.

The transfection protocol for both TransIT-2020 and TransIT-LT1 was as follows: Firstly, 250 μ l of Opti-MEM medium was added to a microcentrifuge tube. Then, 2.5 μ g of DNA was added to the tube, followed by the addition of 7.5 μ l of the transfection reagent. The mixture was incubated at room temperature for 20 minutes to allow stable complex formation. Meanwhile, the medium in the culture dishes was replaced with 2 mL of pure DMEM. After the incubation period, the DNA-transfection reagent mixture was added to the cells.

Incubation, medium change, and/or cell passaging until imaging

Following transfection, a series of workflow optimizations were conducted to identify the most effective post-transfection handling strategy in terms of both cell health and protein expression efficiency, particularly on the day of imaging using confocal and optoacoustic methods. Specifically, three different workflows were designed and tested, as shown in Table 2, each varying in the timing and sequence of key steps such as medium replacement, cell passaging, and imaging. These workflows were intended to balance the rapid proliferation rate of HEK cells with the need for sufficient expression time and optimal cell adhesion.

Table 2: Three different post-transfection workflows tested in HEK cells to evaluate the impact of medium change, cell passaging, and incubation timing on cell health and protein expression efficiency at the time of imaging.

	Day 1	Day2	Day3	Day4	Day 5
1	Cell seeding	Transfection	Medium change	Imaging	/
2	Cell seeding	Transfection	Cell passaging	Incubation	Imaging
3	Cell seeding	Transfection	Cell passaging	Imaging	/

In the table, the term “medium change” refers to the replacement of pure DMEM (used during transfection to avoid interference from serum proteins) with standard culture medium containing 10% FBS. This step was intended to re-establish normal growth conditions and promote robust protein expression post-transfection. For workflows involving cell passaging, cells were detached using standard enzymatic digestion using trypsin, resuspended, and reseeded into new dishes with fresh FBS-containing medium. The passaging protocol followed standard procedures but was adjusted proportionally based on the smaller surface area of the experimental culture dishes (9.6 cm^2) compared to typical cell culture plates (60.1 cm^2). The split ratio (1:2 or 1:3) was chosen depending on the planned imaging schedule, with a goal of achieving 70–80% confluence at the time of imaging, optimal for both cell morphology and signal consistency.

After comparing the outcomes of all three workflows, workflow 2 was determined to be the most effective and was therefore adopted for all subsequent transfection experiments. In this workflow, cells were transfected on Day 2 and passaged on Day 3, with imaging performed on Day 5. This allowed sufficient time for the cells to both recover from transfection and re-adhere to the dish after passaging, ensuring optimal morphology and expression.

In contrast, workflow 1 presented issues with overconfluence. Because the cells were already near 80% confluency at the time of transfection, by the time of imaging on Day 4, the cultures often exceeded 100% confluency. This led to overcrowding, altered morphology (e.g., loss of defined cell borders and flattening), and poor attachment to the dish. When the imaging medium was introduced, many cells detached, leading to significant sample loss and inconsistent imaging results.

Workflow 3, on the other hand, involved passaging one day prior to imaging, but this did not allow enough time for the cells to firmly re-adhere to the culture surface. As a result, during imaging preparation (e.g., medium change or washing), cells were more prone to detachment. This reduced both the number of viable cells and the uniformity of the imaging field.

Taken together, these observations highlight the importance of precisely timed post-transfection handling steps. Workflow 2 strikes a balance between sufficient recovery time, optimal confluency, and strong adhesion, making it the most suitable for sensitive downstream imaging applications. This protocol was therefore adopted as the standard procedure in all following experiments.

Introducing biliverdin, confocal, and OAM imaging

Confocal fluorescence imaging was conducted using a ZEISS LSM 880 Indigo AxioObserver microscope using a 633 nm excitation laser. Fluorescence emission was collected within the spectral range of 643–754 nm to capture the near-infrared signals emitted by the GECI variants. Image acquisition settings were kept consistent across samples to ensure comparability. The acquired images were subsequently analyzed using a combination of ZEISS ZEN software for initial processing, ImageJ (Fiji) for quantitative analysis, and MATLAB for advanced processing and visualization.

For optoacoustic imaging, a customized microscopy setup was employed, as shown in **Figure 7**. A 650 nm pulsed laser beam, generated by a dye laser, was used to illuminate a defined region within the imaging dish. The laser beam was coupled directly into the imaging medium, ensuring full immersion of the beam path to minimize scattering and refraction at the air–liquid interface. The imaging dish contained HEK293-T cells previously transfected with GECI and was positioned at the bottom. A high-frequency ultrasound transducer was aligned above the dish to detect optoacoustic signals generated by the cells upon laser excitation. The transducer was connected to a data acquisition system (DAQ), which recorded the acoustic signals with high temporal precision for subsequent image reconstruction and analysis. The optoacoustic imaging system was controlled by a custom program written in MATLAB.

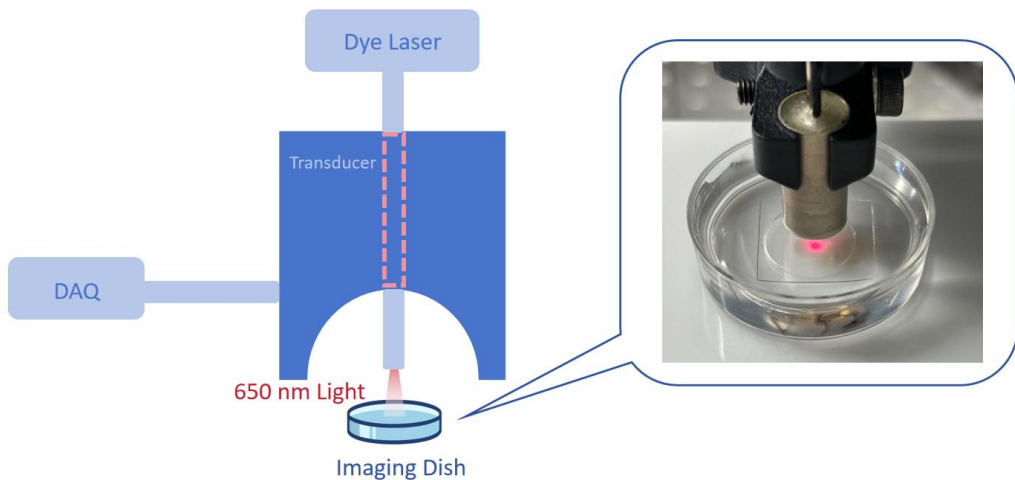


Figure 7: Schematic diagram and photograph of the optoacoustic microscopy system used for imaging transfected HEK cells. A 650 nm light generated by a dye laser is focused on the imaging dish containing the cells. The transducer, positioned above the dish, detects the optoacoustic signals produced by the cells upon laser excitation. The setup is connected to a data acquisition (DAQ) system for recording and analyzing the signals.

For each transfection experiment, three rounds of imaging were conducted to capture a comprehensive dataset: the first confocal imaging, followed by optoacoustic imaging, and a second round of confocal imaging to observe any changes or dynamics over time.

- First confocal imaging: Identify suitable areas for optoacoustic scans and acquire tiling images to create a cell map.

- Optoacoustic imaging: Record optoacoustic responses using a lower-energy laser. In the same field of view, use a higher-energy laser to scan multiple times to induce photobleaching.
- Second confocal imaging: Observe the areas previously scanned with optoacoustic. Compare these images with the initial confocal tiling images to identify photobleached regions, which can serve as alignment references for optoacoustic and confocal imaging.

Creating a photobleaching reference serves two purposes. First, it aids in identifying the optoacoustic-scanned area within the confocal tiling images. Second, once the scanned area is located, the source of the optoacoustic signal can be verified by confirming whether the optoacoustic signal corresponds to features observed in the confocal images. In parallel, efforts will be directed toward improving the confocal and optoacoustic imaging devices to achieve more precise and quantifiable results

Also, for imaging with the codon-optimized GECI sequence in the pAAV backbone, external biliverdin was required to be added to the medium. This was necessary because, in the previously used plasmids (pDuEx and pRSET backbones), the plasmid included the *HO1* gene downstream of the GECI sequence. The *HO1* gene encodes heme oxygenase-1, an enzyme that catalyzes the degradation of heme and produces biliverdin as one of the byproducts. Consequently, in earlier experiments, no external biliverdin source was needed, as the cells could generate sufficient biliverdin from the *HO1* gene activity.

However, with the codon-optimized GECI sequence cloned into the pAAV backbone, the plasmid does not contain the *HO1* gene. As a result, the cells were unable to produce biliverdin endogenously, and external biliverdin had to be added to the medium to ensure proper chromophore binding and enhance protein fluorescence. Two concentrations of biliverdin were tested in this experiment: 12.5 μM and 25 μM , which were chosen based on recommendations from previous literature concerning NIR-GECO1 [9].

For the initial transfection experiments, biliverdin was introduced to the medium 3 hours before the first round of confocal imaging, a time frame suggested by the literature [17].

However, as shown in **Figure 8**, using V8.4 as an example, it was observed that the fluorescence intensity in the second round of confocal imaging was significantly higher compared to the first round, with approximately 7 hours of incubation in between. This increase in fluorescence intensity suggested that a longer incubation period with biliverdin may enhance the chromophore binding and fluorescence expression. Based on these findings, for all subsequent transfection experiments, biliverdin was added to the medium one night prior to the imaging day. This extended incubation period ensured that sufficient time was provided for biliverdin binding and optimal fluorescence signal generation, leading to more consistent and enhanced imaging results.

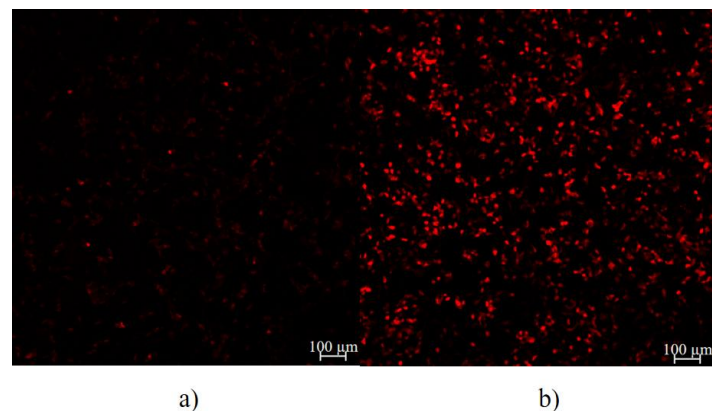


Figure 8: Confocal images of V8.4 at different time points on the imaging day using same imaging parameters when biliverdin was added 3 hours before the first confocal imaging. a) The first confocal imaging, showing low fluorescence intensity. b) The second confocal imaging, after 7 more hours of incubation with biliverdin, demonstrates a significant increase in fluorescence intensity. This enhancement indicates that the longer incubation time allowed for better biliverdin binding, resulting in a stronger fluorescent signal.

2.2 Confocal and optoacoustic imaging in *E. Coli*

To further evaluate the performance of the GECI sensors, both confocal and optoacoustic imaging were conducted in *E. coli* to assess whether the expected calcium response could be reliably observed in a prokaryotic system. A total of 13 imaging experiments were performed, each following the standardized workflow illustrated in **Figure 9**, with the aim of identifying the optimal conditions for achieving robust and reproducible calcium responses during imaging. Firstly, the GECI plasmids were transformed into *E. coli*, followed by incubation until visible colonies were formed and fully matured. Subsequently, the colonies were transferred onto a Whatman filter paper and positioned inside a new Petri dish to facilitate imaging. The detailed imaging setup and preparation protocol are described below. Finally, both confocal and optoacoustic microscopy were performed on the *E. coli* colonies to analyze their fluorescence properties and calcium responsiveness under the experimental conditions.

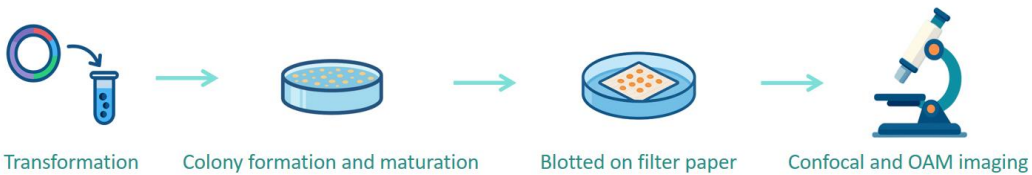


Figure 9: Workflow for bacterial expression and imaging of GECI sensors in *E. coli*. The process begins with transformation of GECI plasmids into *E. coli*, followed by colony formation and overnight maturation at 4 °C to ensure full expression of the sensor. Matured colonies are then blotted onto pre-treated filter paper placed in a Petri dish. Finally, the prepared samples are imaged using both confocal microscopy and optoacoustic microscopy to evaluate sensor functionality.

Transformation

GECI protein variants were individually transformed into *E. coli*. Specifically, plasmids containing each variant in the pRSET expression backbone were introduced into T7 Express Competent *E. coli* (strain C2566H) using the standard transformation protocol described below:

Firstly, all DNA samples of protein variants were diluted to a concentration range of 5 – 10 ng/µL using Milli-Q water. Then, 5 µL of the diluted DNA was transferred into 25 µL of freshly thawed *E. coli* competent cells. The mixture was incubated on ice for 30 minutes to allow DNA adsorption into the bacteria, followed by an additional 10-minute incubation at

room temperature to enhance transformation efficiency. Finally, the transformed *E. coli* cells were plated onto LB agar plates containing 400 mg/L Ampicillin (Amp) for selection. The plates were then incubated at 37°C overnight to allow colony formation.

Imaging preparation

After overnight incubation at 37 °C, the *E. coli* colonies were further incubated at 4 °C for 24 hours to allow full maturation of the expressed GECI sensors. To prepare the samples for imaging, a portion of the matured *E. coli* colonies was gently blotted onto a piece of Whatman 3MM filter paper that had been pre-soaked with calcium-free HBSS- buffer. The filter paper was then carefully placed inside a sterile 9.6 cm² Petri dish. To immobilize the bacterial colonies and prevent displacement during imaging, 1 mL of molten 0.5% (w/w) agar was overlaid onto the filter paper and allowed to solidify.

For optoacoustic imaging, efficient acoustic coupling was essential. To achieve this, a sufficient volume of calcium-negative buffer was added to the Petri dish, ensuring full submersion of the agar-embedded sample. For confocal imaging, the buffer is composed of 30 mM MOPS, 100 mM KCl, and 10 mM EGTA (pH 7.2). For optoacoustic imaging, phosphate-buffered saline (PBS) was used instead.

To saturate the calcium sensors expressed in *E. coli*, a two-step protocol was tested first. First, a permeabilization solution containing poly-D-lysine and ionomycin (each at 50 µg/mL in HBSS- buffer) was applied for 5 minutes. Ionomycin, a calcium ionophore, facilitates the transmembrane transport of Ca²⁺ into cells. Poly-D-lysine, a positively charged polymer, enhances cell adhesion to the substrate and may also promote membrane permeability in bacterial cells by interacting with the negatively charged components of the cell wall. Following this treatment, a calcium-positive solution consisting of 30 mM MOPS, 100 mM KCl, 10 mM EGTA, and 10 mM CaCl₂ (adjusted to pH 7.2, yielding a free calcium concentration of 39 µM) was applied to fully activate the calcium sensors.

However, under this setup, no calcium-induced fluorescence or optoacoustic response was observed. It was hypothesized that the agar layer may have acted as a physical barrier, limiting

the penetration of ionomycin and calcium ions into the *E. coli* colonies. Consequently, for subsequent experiments, the pre-soaking step was modified: instead of HBSS- buffer alone, the filter paper was pre-soaked directly in the poly-D-lysine and ionomycin solution (50 $\mu\text{g}/\text{mL}$ each in HBSS-). This adjustment aimed to improve reagent access and facilitate more effective calcium ion transport into the bacterial cells during imaging. The final setup is shown in **Figure 10** below:

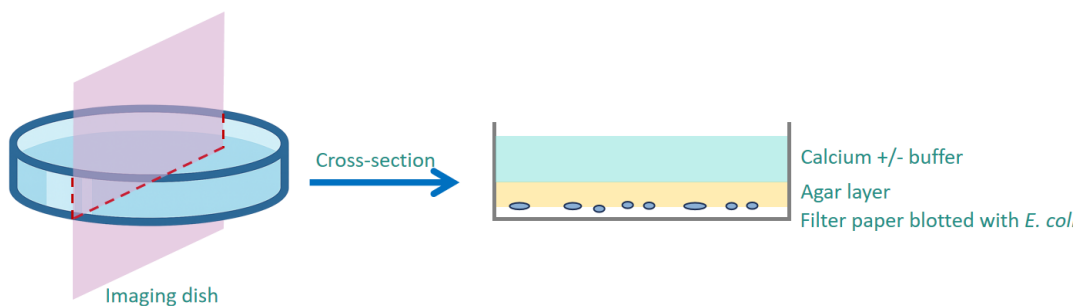


Figure 10: Schematic cross-sectional view of the *E. coli* imaging setup. After blotting *E. coli* colonies onto a filter paper, the paper was placed at the bottom of an imaging dish. A thin agar layer was applied to immobilize the colonies, followed by the addition of calcium-positive or calcium-negative buffer to ensure proper acoustic coupling during imaging and to enable assessment of calcium responsiveness.

Confocal and OAM imaging

The prepared Petri dishes were subjected to both confocal and optoacoustic microscopy for comprehensive imaging analysis. Confocal imaging was conducted using a ZEISS Axio Observer.Z1/7 microscope, utilizing the AF647 dye to visualize protein expression. The excitation wavelength was set to 653 nm, and fluorescence emission was detected within the 656–700 nm range to optimally capture the near-infrared fluorescence signal. All imaging parameters were maintained consistently across experimental groups to ensure reliable comparisons. The optoacoustic image followed the same setup as described in section 2.1. The acquired images were subsequently processed and analyzed using ZEISS ZEN software, ImageJ, as well as MATLAB for additional data analysis, plotting, and customized computational workflows.

2.3 Protein purification

GECI proteins were purified following a multi-step process, as illustrated in **Figure 11**. Initially, the GECI plasmids were transformed into *E. coli* using standard transformation protocols. After successful transformation, individual colonies were picked and cultured in a small-scale Miniculture, followed by a larger-scale Maxiculture to produce sufficient bacterial biomass. The cells were then harvested by centrifugation to separate the bacterial pellet from the culture medium.

Subsequently, the GECI proteins were extracted from the *E. coli* using a French Press, a mechanical cell disruption technique that efficiently lyses the bacterial cells, releasing the intracellular proteins. The crude protein extract was then subjected to affinity chromatography using a suitable column (HisTrap) to purify the GECI proteins based on their histidine tags. This purification process ensures the isolation of high-purity GECI proteins for further characterization and analysis. Below is a detailed explanation of each step in the procedure.



Figure 11: Schematic representation of the GECI protein purification process. The procedure begins with the transformation of GECI plasmids into *E. coli*. After successful transformation, individual colonies are picked and cultured in Miniculture followed by Maxiculture. The bacterial cells are then collected by centrifugation, and protein extraction is carried out using a French Press. Finally, the GECI proteins are purified through affinity chromatography to obtain high-purity protein for subsequent analysis.

Transformation

Firstly, all four protein variants (NIR-GECO3, V5.2, V6.2, and V8.4) were transformed into *E. coli*. To evaluate the differential protein expression efficiency associated with plasmid backbones and *E. coli* strains, two expression systems were tested for each variant, with the exception of NIR-GECO3. Specifically, for V5.2, V6.2, and V8.4, pRSET plasmid carrying the variant was transformed into T7 Express Competent *E. coli* (strain C2566H), and pDuEx2

plasmid carrying the variant was transformed into DH10B Competent *E. coli*. Due to the unavailability of a pRSET-based construct for NIR-GECO3, only the pDuEx2 plasmid carrying this variant was transformed into DH10B cells. This experimental design allowed for a comparative analysis of backbone-strain combinations in terms of their impact on protein expression.

Regarding induction, in theory, isopropyl β -D-1-thiogalactopyranoside (IPTG) can be used to induce the expression of T7 RNA polymerase in T7 Express Competent *E. coli*, as its expression is controlled by the lac promoter. The expressed T7 polymerase subsequently activates transcription from the T7 promoter located upstream of the GECI gene in the pRSET plasmid, thereby driving GECI protein expression. Additionally, IPTG is also capable of inducing GECI expression when the gene is under the control of the tac promoter in the pDuEx2 plasmid backbone, due to the lac operator elements present in this system. Also, since GECI needs biliverdin as a chromophore to absorb light, external biliverdin could be applied to support proper chromophore formation and protein maturation.

However, no IPTG induction was applied and no biliverdin was added to the LB agar plates, as blue colonies were already observed in the absence of inducer and biliverdin. The appearance of blue colonies indicated that basal expression from the promoter was already sufficient for a detectable level of GECI protein to be expressed, and that a sufficient amount of biliverdin was endogenously produced by the activity of the HO1 enzyme, which is encoded downstream of the GECI coding sequence and catalyzes the conversion of intracellular heme into biliverdin. In contrast, when IPTG was added, colony growth was notably suppressed, which was likely due to the toxicity associated with the overexpression of GECI proteins under induced conditions.

Subsequently, the transformation of GECI plasmids into *E. coli* was carried out following the same procedure described in Section 2.2.

Miniculture and Maxiculture

After incubation, for each plate, three individual colonies were randomly picked and transferred into 4 mL of LB liquid medium containing 100 mg/L ampicillin to establish

minicultures. These minicultures were incubated at 37 °C with shaking at 208 rpm for 8 hours to allow for sufficient bacterial growth and protein expression. After this incubation period, of the same protein variant, the intensity of the blue coloration in each culture was visually compared to assess the relative expression level of the GECI protein.

It was found that, for the protein variants V5.2, V6.2, and V8.4, the combination of the pRSET plasmid with T7 Express Competent *E. coli* generally resulted in a higher intensity of blue color compared to the combination of the pDuEx2 plasmid with DH10B cells. This observation suggests that the expression system utilizing the T7 promoter in the T7 Express strain may offer enhanced transcriptional efficiency under non-induced conditions.

Among the minicultures derived from the same plate, the one displaying the most intense blue coloration was selected and 1 mL of miniculture was transferred into a 1000 mL Erlenmeyer flask containing 250 mL of LB liquid medium for maxiculture. The maxiculture was incubated at 37 °C with shaking at 208 rpm for 20 hours to allow for extended protein production.

Harvest bacteria

After maxiculture, the resulting cultures of each protein variant are shown in **Figure 12**. The intensity of the blue coloration provides a rough visual indication of the relative concentration of GECI proteins expressed in each culture. It can be observed that, in general, the variants V5.2, V6.2, and V8.4 exhibited higher expression levels compared to NIR-GECO3. This difference is likely attributable to the more efficient combination of the pRSET plasmid with T7 Express Competent *E. coli*, which may offer enhanced transcriptional activity and protein production capacity under the conditions used in this study.

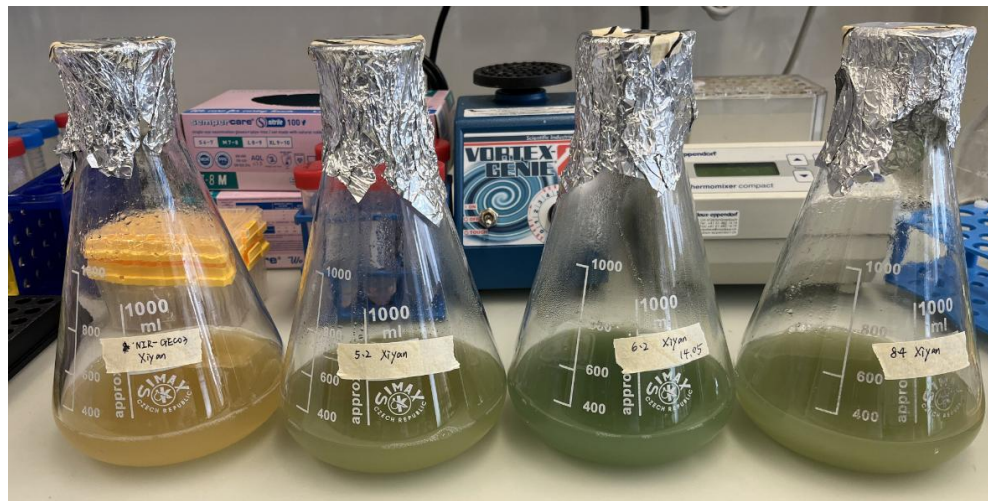


Figure 12: Maxiculture of each GECI protein variants. From left to right: NIR-GECO3, V5.2, V6.2, V8.4. In general, the variants V5.2, V6.2, and V8.4 exhibited higher expression levels compared to NIR-GECO3.

The bacterial culture medium was then collected and centrifuged at 4000 rpm at 4 °C for 25 minutes to pellet the cells. The supernatant was carefully discarded, and the resulting bacterial pellet was resuspended in 15 mL of Low Imidazole buffer (20 mM imidazole dissolved in a general buffer composed of 5 M NaCl, 1 M Na₂HPO₄, and 1 M NaH₂PO₄ prepared in Milli-Q water). The resuspension was performed thoroughly to ensure uniform mixing and to facilitate subsequent lysis. The resuspended bacterial suspension was then stored at -20 °C overnight.

Protein extraction from bacteria

After overnight incubation, the resuspended bacterial suspension was removed from -20°C and placed on ice to allow for slow thawing while preparing and setting up the French Press. The bacterial cells were then broken up by passing the suspension through the French Press. To minimize potential cross-contamination between the protein variants, the break-up process was performed in order of increasing protein concentration, based on the assumption that the intensity of the blue color correlates with the concentration of GECI protein. Thus, the process started with the least colored (lower concentration) bacteria and progressed to the more intensely colored (higher concentration) samples.

Following the break-up, for the protein variants V5.2, V6.2, and V8.4, the lysed cell suspension was passed through a 26G needle attached to 20 mL syringe once and aliquoted into

ten 2 mL Eppendorf tubes, with 1.5 mL in each tube. This step was done to reduce the viscosity of the suspension and to avoid clogging the column during subsequent purification. This viscosity reduction step was unnecessary for NIR-GECO3, as its product was less viscous, likely due to the lower bacterial yield.

After aliquoting, all protein variants (NIR-GECO3, V5.2, V6.2, and V8.4) were subjected to centrifugation at 13,000 rpm for 3 minutes to remove bacterial debris. The supernatant was then carefully collected, while pellets lacking blue coloration were observed, confirming that the GECI proteins had been successfully collected into the supernatant. This observation ensured that the majority of the expressed proteins were present in the soluble fraction, making them ready for downstream purification.

Protein purification with column

A HisTrap FF column was equilibrated by passing 5 mL of water through the column, followed by 5 mL of Low Imidazole buffer, at a flow rate of 1 *mL/min*. During the loading of the protein sample onto the HisTrap FF column, any bubbles or foam were minimized by tapping gently on the column entrance and ensuring that the column was fully filled with an excess of liquid. After equilibration, the protein samples were loaded and passed through the column at a flow rate of 0.5 *mL/min*. Following the loading, the column was washed with 15 mL of Low Imidazole buffer at a flow rate of 1 *mL/min* to remove unbound material. The protein was then eluted using 5 mL of High Imidazole buffer (220 *mM* imidazole dissolved in general buffer) at a flow rate of 0.3 *mL/min*.

For protein collection, three metal chelate (MC) fractions were collected for each protein sample. MC1 was collected starting from the first drop that showed a blue color, which was detected by observing the flow of the blue color through the column. MC2 was collected when approximately 500 μL of MC1 had been collected and when the color intensity dropped significantly. MC3 was collected when the drops exiting the column appeared almost colorless or very faintly blue, and collection was stopped once the color had completely disappeared, usually with only four drops collected. After collecting MC1–3, the flow rate was increased to

1 mL/min (the maximum flow rate) to allow any remaining high imidazole buffer to flow into waste.

If the column was to be reused for processing other protein samples on the same day, it was re-equilibrated by passing 5 mL of water through the column, followed by 5 mL of Low Imidazole buffer at a flow rate of 1 mL/min. For long-term storage of the column, the column was washed with 5 mL of water at 1 mL/min, followed by equilibration with 5 mL of 20% ethanol at 1 mL/min.

After the collection of MC1–3, the protein fractions were further processed using a PD MiniTrap G-25 size exclusion column (Cytiva), which was equilibrated with Tris/NaCl buffer (1 M *Tris/HCl* (pH 7.4), 5 M *NaCl* in Milli-Q water). The column was filled with Tris/NaCl buffer to its maximum volume and allowed to empty by gravity. Once the column was equilibrated, approximately 450 μ L of MC1 was carefully loaded onto the column. The sample volume should not exceed 500 μ L to avoid contamination of the eluate with imidazole. Once the sample had completely entered the column bed, the column was washed with 0.2 mL of Tris/NaCl buffer. Elution was then carried out with 0.5 mL of Tris/NaCl buffer (fraction SE1), followed by 0.2 mL of Tris/NaCl buffer (fraction SE2). The elution volume could be adjusted based on the position of the blue color in the collected fractions. Finally, the initial protein concentration and absorbance spectra were measured using a Nanodrop spectrophotometer in the Protein A280 mode. This method allows for a quick and rough estimate of the protein concentration based on absorbance at 280 nm.

2.4 Protein characterization

The general workflow for protein characterization is shown in **Figure 13**. Before proceeding with detailed characterization, the concentrations of the four purified GECI protein variants (NIR-GECO3, V5.2, V6.2, and V8.4) were first accurately quantified using spectrophotometric measurements, ensuring consistency across samples for comparative analysis. Once normalized, the proteins underwent a comprehensive evaluation of their fluorescence and optoacoustic properties to assess the effects of directed evolution.

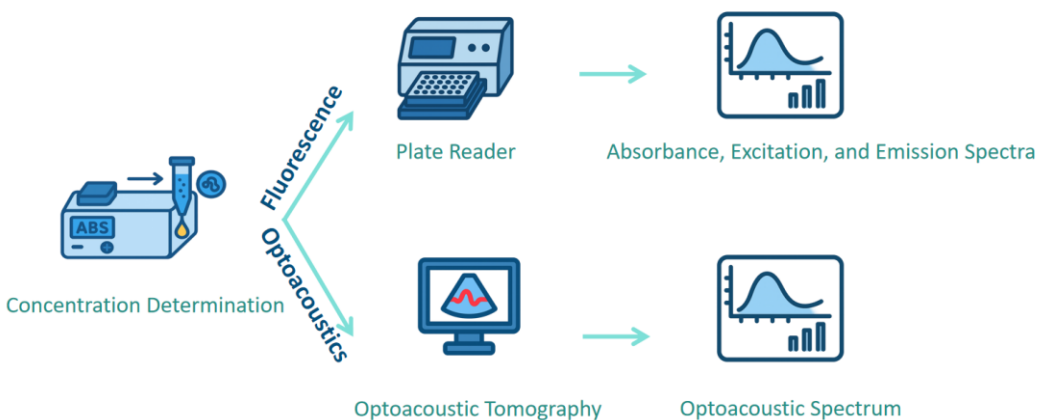


Figure 13: Workflow for fluorescence and optoacoustic characterization of GECI proteins. After determining protein concentrations, purified GECI samples undergo two parallel characterization pipelines. For fluorescence-based analysis, a plate reader is used to measure absorbance, excitation, and emission spectra. In parallel, optoacoustic tomography is employed to evaluate the optoacoustic spectrum. These pathways reflect the two primary fates of absorbed light energy, either conversion into fluorescent emission or into ultrasound via thermoelastic expansion, providing complementary insights into the optical and optoacoustic performance of the biosensor.

For fluorescence-based characterization, key spectral features, including absorbance, excitation, and emission spectra, were measured using a multi-mode plate reader. These measurements helped determine each variant's fluorescence intensity and calcium sensitivity under varying conditions, which are critical for their effectiveness as optical indicators.

Importantly, as suggested in **Figure 14**, the light absorbed by the protein chromophore (as measured by absorbance) is subsequently converted either into fluorescence emission (measured via the emission spectrum) or into acoustic pressure waves (captured as optoacoustic

signals). The partitioning of this absorbed energy determines the signal strength and modality sensitivity of the reporter protein.

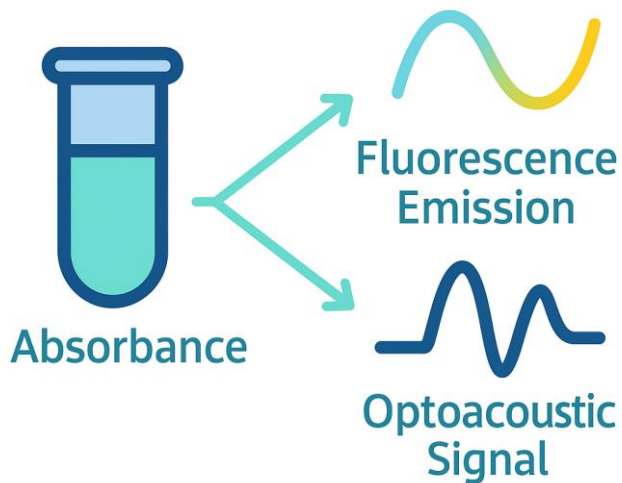


Figure 14: Schematic illustration of light energy conversion pathways in GECI proteins. Upon absorbing light (measured by absorbance), GECI proteins can convert the absorbed optical energy into either fluorescent emission (measured by emission spectra) or acoustic waves through thermoelastic expansion (measured by optoacoustic signal). The balance between these two energy conversion routes depends on the protein's quantum yield and non-radiative relaxation efficiency, which are crucial for optimizing its performance in fluorescence and optoacoustic imaging.

For optoacoustic characterization, the same protein variants were analyzed using an optoacoustic tomography system. This setup allowed for the measurement of optoacoustic spectra under both calcium-free and calcium-loaded conditions, providing insight into the protein's potential as calcium-responsive contrast agents in photoacoustic imaging.

Together, these characterizations provided a comprehensive understanding of how directed evolution altered the optical and acoustic properties of each GECI variant, laying the groundwork for their future application in deep-tissue functional imaging.

Protein concentration determination

In order to characterize and compare the properties of different protein variants, the protein concentration after purification was determined to ensure that the same concentration could be maintained during subsequent characterization and comparison experiments. Protein concentration was calculated based on the absorbance at 280 nm, as measured by the Nanodrop spectrophotometer. The relationship between absorbance and protein concentration is described by the Beer-Lambert Law, which is summarized in Equation 1 below. This law provides a linear

relationship between absorbance and concentration, allowing for accurate quantification of the protein based on its UV absorbance.

$$A = \epsilon \cdot c \cdot l \text{ (Equation 1)}$$

Where:

- a) A = Absorbance (unitless), which represents the protein's absorption of light at around 280 nm in the UV range, measured as A280 using the Nanodrop spectrophotometer. This absorbance is primarily attributed to aromatic amino acids, especially tryptophan, due to the conjugated pi electrons in their aromatic rings. Since GECI proteins contain a sufficient amount of tryptophan, this relationship is considered reliable. During calculation, the actual absorbance was determined by subtracting the background absorbance (measured in high imidazole solution) from the protein's absorbance value.
- b) ϵ (epsilon) = Molar Extinction Coefficient (Unit: L·mol⁻¹·cm⁻¹) at 280 nm measured in water, which is also referred to as molar absorption coefficient or molar absorptivity. This constant indicates the substance's ability to absorb light at a specific wavelength. It is a protein-specific property, and for our proteins, it was obtained using ProtParam by submitting the protein sequence. For the purpose of this study, it was assumed that all cysteine residues were in their reduced form.
- c) c = Concentration of the protein (Unit: mol/L), which is the value to be calculated.
- d) l = Path length of the cuvette (Unit: cm). Typically, the standard path length for cuvettes is 1 cm.

With the protein concentration calculated for each variant after purification, all proteins were diluted to the same concentration for characterization.

Absorbance, excitation, and emission spectra determination

All purified protein variants were diluted to a concentration of 3 μ M using a buffer solution. For each protein variant, two distinct dilution conditions were prepared to examine the effect of calcium binding on the protein properties. One condition utilized a calcium-positive buffer consisting of 30 mM MOPS, 100 mM KCl, 10 mM EGTA, and 10 mM Ca^{2+} ,

resulting in a final calcium concentration of $39 \mu M$ at pH 7.2. The second condition used a calcium-negative buffer with the same composition, excluding the calcium ions, to serve as a control for comparison. The goal of this experimental setup was to investigate how the presence or absence of calcium ions influences key protein properties, specifically absorbance, excitation, and emission spectra.

Once the proteins were diluted in both buffers, the protein solutions were transferred into a NuncTM 384-Well Plate (Thermo Fisher), with $50 \mu L$ of each diluted protein solution being added to individual wells for measurement. The spectral properties of the proteins were measured using a Tecan Plate Reader Infinite 200Pro. To ensure the accuracy and reliability of the results, each protein variant was measured five times, providing multiple data points to reduce the impact of random errors and enhance the statistical reliability of the observations.

The critical experimental parameters used for the spectral measurements, including starting wavelength, ending wavelength, and the stepsize, are summarized in Table 3. After data collection, the obtained spectral data were processed, analyzed, and plotted using custom MATLAB code, allowing for clear visualization and interpretation of the effects of calcium binding on the protein characteristics.

Table 3: Parameters used to determine the absorbance, excitation, and emission spectra

	Wavelength Start (nm)	Wavelength End (nm)	Step Size (nm)	Excitation Wavelength (nm)	Emission Wavelength (nm)
Absorbance	300	800	2	/	/
Excitation	500	690	2	/	710
Emission	650	750	2	630	/

Optoacoustic spectra determination

A customized optoacoustic tomography setup was constructed to characterize the optical absorption properties of GECIs. As illustrated in **Figure 15**, the system consisted of a tunable Optical Parametric Oscillator (OPO) laser (wavelength: 650 nm; output energy at fiber: 3.4 mJ),

which was coupled to a fiber bundle to provide top-down illumination onto the sample. The sample was contained within a transparent tube embedded in a 1.3% (w/w) agar matrix prepared using Milli-Q water. The tube passed horizontally through the agar, ensuring acoustic coupling with the underlying transducer. Protein samples were loaded into the tube and aligned with the laser focal zone. A spherical array transducer composed of 256 ultrasound elements was positioned beneath the agar layer and faced upward to detect optoacoustic signals. The transducer was interfaced with a data acquisition (DAQ) system for synchronized signal capture.

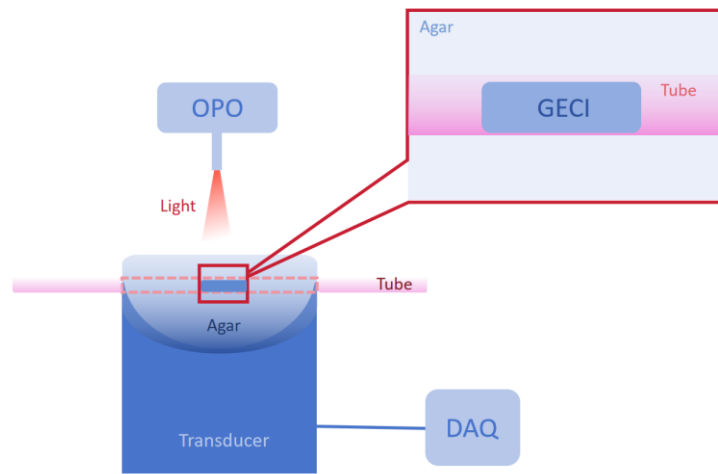


Figure 15: Schematic of the experimental setup for optoacoustic tomography for GECI protein characterization. The OPO laser illuminates the sample inside the tube, which is immersed in agar. The transducer beneath the agar detects the optoacoustic signal, and the DAQ system is connected to record the signals for subsequent analysis.

Prior to protein measurements, system calibration was performed using a stock solution of ink diluted 200-fold in Milli-Q water. This calibration ensured accurate normalization of optoacoustic signals across the wavelength range. First, the optical absorbance of the diluted ink solution was measured using a microplate reader to serve as a reference. Subsequently, the same sample was imaged using the optoacoustic system. Assuming the relationship $OA = F \times Abs$ (where OA is the optoacoustic signal, F is the local optical fluence, and Abs is absorbance), the wavelength-dependent fluence correction factor was calculated by dividing the optoacoustic signal by the absorbance for each wavelength. This wavelength-resolved fluence profile was then used to normalize all subsequent GECI protein measurements.

GECI variants (V5.2, V6.2, V8.4) were each diluted to a final concentration of 60 μM in either calcium-positive or calcium-negative buffers. Same as the buffer used for the plate reader, the calcium-positive buffer consisted of 30 mM MOPS, 100 mM KCl, 10 mM EGTA, and 10 mM Ca^{2+} , resulting in a free calcium concentration of 39 μM at pH 7.2. The calcium-negative buffer had the same composition but excluded calcium, serving as a control to evaluate calcium-dependent optical response. After each sample measurement, the tube was thoroughly washed with Milli-Q water to avoid cross-contamination. Spectral measurements were performed across the 500–680 nm range, using either 2 nm or 5 nm wavelength increments (500:2:680 or 500:5:680).

All optoacoustic data were processed using scripts written in MATLAB. Raw signals were first baseline-corrected and normalized using the previously computed wavelength-specific fluence values. Spectra for each protein condition (calcium-bound vs. unbound) were generated and compared to assess calcium responsiveness and spectral shifts.

Chapter 3: Results and Discussion

3.1 Confocal imaging in HEK293-T cells

Effects of directed evolution

To evaluate the impact of directed evolution, the mean gray values, which represent the average fluorescence intensity, were quantified from tiled confocal microscopy images and compared across four groups: the control group (transfected with a plasmid lacking the GECI insert), and the three evolved variants V5.2, V6.2, and V8.4. This comparison was made under the assumption that the cell density was consistent across all dishes for each protein variant. This assumption is valid because all cells were cultured and transfected under identical conditions, ensuring uniform growth and treatment. Additionally, the different GECI variants did not exhibit significant differences in terms of cellular toxicity. The results of this analysis are summarized in Table 4.

It is evident from the data that the average fluorescence intensity increases with directed evolution. Although the primary focus of the directed evolution process was not fluorescence intensity, but rather absorbance and optoacoustic signal, the observed increase in fluorescence intensity is expected. This is due to the fact that higher absorbance correlates with both increased fluorescence and optoacoustic signal. These findings further support the conclusion that the directed evolution process is effective, as it led to a noticeable enhancement in both absorbance and fluorescence intensity across the protein variants.

Table 4: Average fluorescence intensity of the different GECI variants and the control group

	Control	V5.2	V6.2	V8.4
Average FL intensity	0	3.214	3.866	4.662

Calcium reaction

Since all protein variants (V5.2, V6.2, and V8.4) were derived from the parental sensor NIR-GECO3, they are expected to exhibit a negative correlation between fluorescence intensity and intracellular calcium concentration. In other words, the fluorescence should be brighter

under low calcium conditions and decrease upon calcium binding. To evaluate this calcium responsiveness in HEK cells, time-lapse confocal imaging was performed for each variant. Each imaging cycle had a frame interval of 943.72 ms, and the microscope's detector gain was carefully adjusted for each variant to bring the brightest regions close to saturation. This ensured that changes in fluorescence could be clearly captured upon calcium addition.

During the recording, 40 μL of calcium solution was added to the cells, consisting of 34 μL HBSS- buffer, 4 μL 500 mM CaCl_2 , and 2 μL 1.5 mM ionomycin. Ionomycin acts as a calcium ionophore that facilitates the rapid transport of calcium ions across the plasma membrane, leading to a controlled elevation of intracellular calcium concentration. This process triggers the conformational change of the calcium-sensing domain in the GECI, resulting in a measurable change in fluorescence intensity. The mean fluorescence intensity for each frame in the time series was quantified using ImageJ and plotted against time to visualize the fluorescence dynamics. For comparison across variants, the baseline fluorescence intensity was normalized to 1. The results are shown in **Figure 16** below.

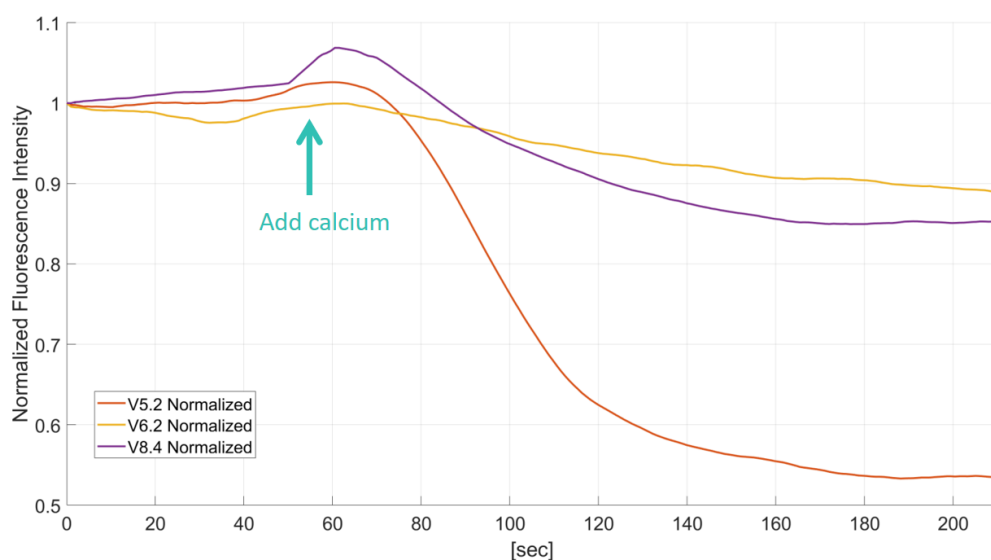


Figure 16: Calcium-induced fluorescence response of GECI variants V5.2, V6.2, and V8.4 in HEK293-T cells. Mean fluorescence intensity was monitored over time during confocal imaging. 40 μL of calcium solution was added at the indicated time point to induce calcium influx. All three variants showed a fluorescence decrease upon calcium addition, consistent with the expected inverse calcium-fluorescence relationship. V5.2 exhibited the largest absolute drop in fluorescence, while V6.2 and V8.4 showed smaller but still evident responses.

As shown above, all three variants exhibited a decrease in fluorescence intensity upon calcium addition, consistent with the expected behavior of NIR-GECO3-derived sensors. Among the variants, V5.2 showed the largest absolute change in fluorescence intensity. In comparison, V6.2 and V8.4 showed similar and more moderate decreases.

This trend is in agreement with the *in vitro* fluorescence characterization results presented later in section 3.4, where the emission spectra of the purified proteins were measured under calcium-free and calcium-saturated conditions. These findings suggest that V5.2 is the most calcium-sensitive variant in terms of fluorescence response. However, since the directed evolution pressure was focused on maximizing the calcium-dependent optoacoustic signal change, it is plausible that the fluorescence sensitivity may not have been directly optimized in later variants. Thus, although V6.2 and V8.4 may show enhanced optoacoustic performance, their calcium-dependent fluorescence response appears to be attenuated compared to the earlier variant V5.2.

To further investigate the reversibility of calcium-induced fluorescence changes, the fluorescence intensity of a single HEK293-T cell transfected with V8.4 was continuously recorded over the course of 450 imaging cycles, using the same confocal imaging parameters as previously described. The result is shown in **Figure 17**. At cycle 90, 40 μL of calcium solution was added to induce a rise in intracellular calcium concentration. As expected, this led to an ~18% decrease in fluorescence intensity due to calcium binding.

To assess whether this decrease was reversible, 40 μL of an Ethylene Glycol Tetraacetic Acid (EGTA) solution (containing 18 μL HBSS- buffer, 20 μL 200 mM EGTA, and 2 μL ionomycin) was introduced at cycle 280. EGTA acts as a calcium chelator, effectively sequestering free calcium ions and thereby lowering the intracellular calcium concentration. Following EGTA addition, the fluorescence intensity gradually increased and eventually returned to near-baseline levels. These results confirm that the fluorescence change induced by calcium binding is reversible, reinforcing its potential utility as a dynamic calcium sensor.

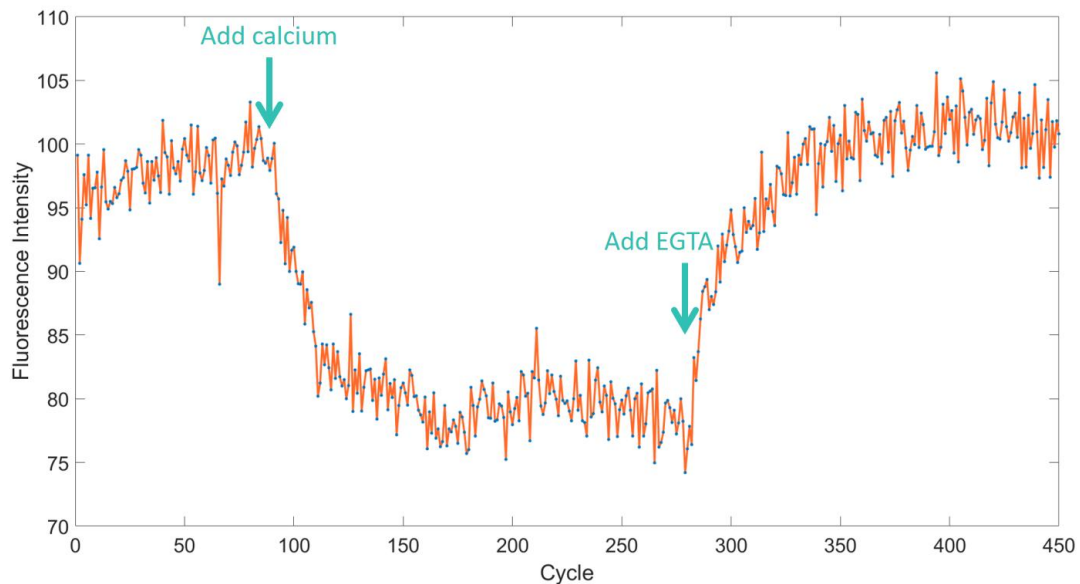


Figure 17: Reversible fluorescence response of V8.4 variant in HEK cells upon calcium addition and subsequent chelation with EGTA. A single HEK cell transfected with V8.4 was imaged over 450 cycles to investigate the reversibility of calcium-induced fluorescence changes. Calcium solution was added at cycle 90, resulting in an ~18% decrease in fluorescence intensity. At cycle 280, 40 μ L of EGTA solution was introduced to chelate intracellular calcium. The fluorescence intensity gradually returned to baseline, confirming the reversible calcium responsiveness of the sensor.

3.2 Optoacoustic imaging in HEK293-T cells

Unexpected calcium response

The most unexpected observation in optoacoustic imaging was the calcium response, which differed significantly from the expected results and from the calcium reaction seen in confocal microscopy. The same calcium and EGTA solutions were used in both imaging modalities, but the outcomes were quite distinct.

As shown in **Figure 18** below, the results are presented for V6.2 using different concentrations of biliverdin ($12.5 \mu M$ and $25 \mu M$). From top to bottom, the images show the optoacoustic signals before any treatment (original), after adding $40 \mu L$ calcium solution, and after adding $40 \mu L$ EGTA solution. A key observation is that in the leftmost column, no detectable optoacoustic signal was observed, which is consistent with the imaging results of other protein variants. This is likely due to the signal being too weak to be captured from a monolayer of HEK cells under the current imaging conditions. These findings suggest that further optimization of GECIs is needed to enhance optoacoustic signal output, enabling more robust detection in future experiments.

Unexpectedly, the optoacoustic signal increased by more than 10-fold after the addition of calcium and decreased again after EGTA was added, which is the opposite of the anticipated response. Additionally, the extent of the signal increase following calcium addition was positively correlated with the biliverdin concentration in the dish. This observation suggests that the biliverdin may have a significant influence on the unexpected optoacoustic signal response.

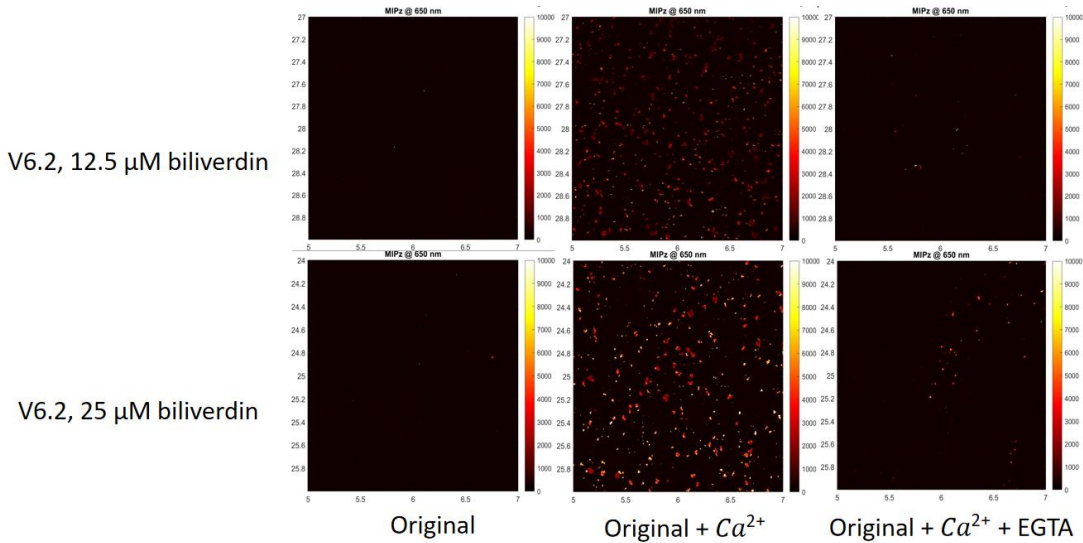


Figure 18: Optoacoustic imaging of V6.2 with different biliverdin concentrations. The images are displayed from top to bottom with biliverdin concentrations of $12.5 \mu M$ (top row) and $25 \mu M$ (bottom row). From left to right: the first column shows the original image before adding any reagents, the second column shows the image after adding $40 \mu L$ calcium solution, and the third column shows the image after adding $40 \mu L$ EGTA solution. Unexpectedly, the optoacoustic signal increased by more than 10-fold after adding calcium, and decreased again after EGTA addition, which was the opposite of the expected result. Additionally, the increase in optoacoustic signal upon calcium addition was found to be positively correlated with the biliverdin concentration in the dish.

To investigate the cause of the unexpected calcium response observed, a series of control experiments were conducted to determine whether the observed effects were due to the GECI protein or other factors. Specifically, a V6.2 dish without biliverdin was tested, alongside two control dishes with $25 \mu M$ biliverdin. The first control dish was transfected with the same plasmid but without the GECI insertion, while the second control dish was not transfected with any plasmid.

The optoacoustic imaging results are shown below. **Figure 19** presents the optoacoustic image of V6.2 without adding biliverdin. It was observed that when biliverdin was not included, the unexpected calcium response was not observed. Additionally, the signal intensity did not change significantly, whether or not Ca^{2+} or EGTA was added. These findings suggest that the observed optoacoustic signal changes in V6.2 were likely influenced by the presence of biliverdin, confirming that biliverdin plays a critical role in this unexpected calcium response.

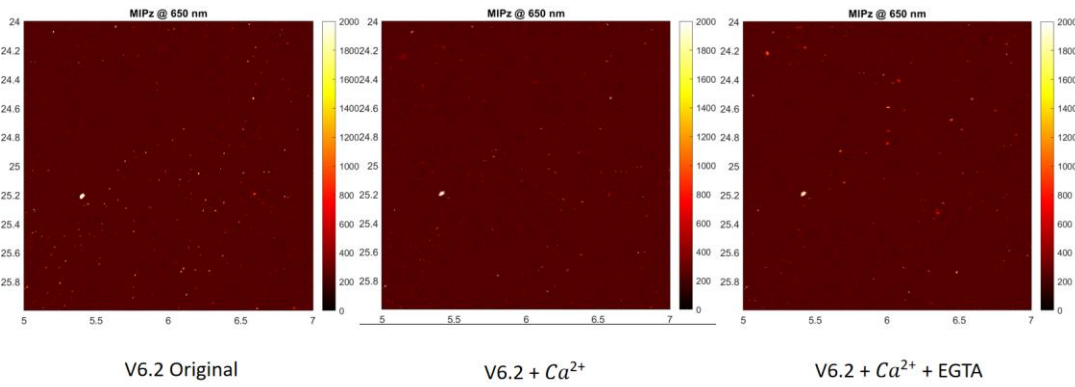


Figure 19: From left to right: The original image of V6.2 without adding any reagents (Original), the image after adding Ca^{2+} to the medium ($\text{V6.2} + \text{Ca}^{2+}$), and the image after adding EGTA to remove calcium ($\text{V6.2} + \text{Ca}^{2+} + \text{EGTA}$). These images reveal that the calcium response in the absence of biliverdin did not show significant signal changes with the addition of Ca^{2+} or EGTA. These results suggest that the observed calcium reaction in V6.2 is dependent on the presence of biliverdin, highlighting its role in this unexpected calcium response.

The optoacoustic results for the two control dishes with $25 \mu\text{M}$ biliverdin were identical.

Figure 20 shows the images for the control dish that was not transfected, but had $25 \mu\text{M}$ biliverdin added. In this case, the same unexpected calcium response was observed, with the optoacoustic signal increasing after the addition of Ca^{2+} and decreasing after EGTA. Based on these results, it became clear that the observed effect was not due to the GECI protein itself, but rather the presence of biliverdin, which seems to play a significant role in the calcium response.

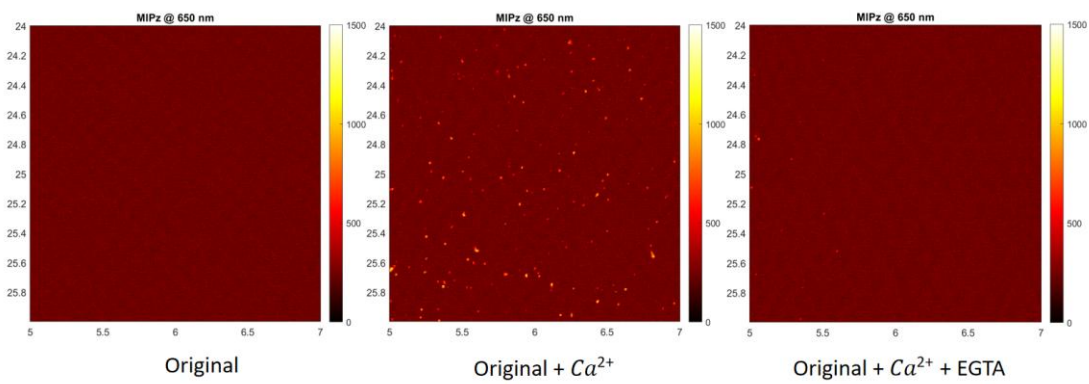


Figure 20: Optoacoustic imaging of the control dish with $25 \mu\text{M}$ biliverdin, showing the same unexpected calcium response observed in the experimental dishes. From left to right: Original image before adding any reagents, image after adding Ca^{2+} , image after the addition of EGTA. As with the experimental dishes, the optoacoustic signal increased after the addition of Ca^{2+} and decreased after EGTA treatment. These findings confirm that the observed response is driven by biliverdin, not the GECI protein.

To further investigate the cause of the observed calcium response, a control dish with HEK cells (without transfection) was prepared and subjected to calcium treatment. The cells were then directly observed under the confocal microscope to determine if any visible changes occurred. Surprisingly, black precipitates were observed after the addition of the calcium solution, which disappeared after adding EGTA. These observations are shown in **Figure 21** below. Notably, the formation of the precipitate occurred regardless of the imaging medium used, whether it was DMEM supplemented with FBS, HBSS-, or Milli-Q water.

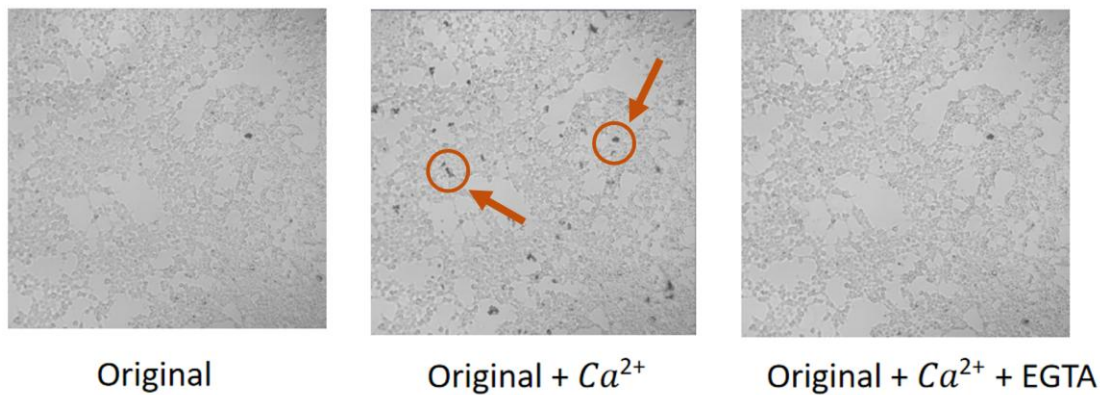


Figure 21: Optical images of the control dish with HEK cells (without transfection) before and after calcium treatment. From left to right: The cells before any treatment, the cells after adding the calcium solution, where black precipitates are observed. The third image (Original + Ca^{2+} + EGTA) shows the cells after adding EGTA, where the precipitates have disappeared. These observations suggest that the black precipitates are formed through a chemical reaction between biliverdin and calcium solution, which produces a strong optoacoustic signal upon calcium addition.

Based on these findings, it can be conjectured that the black precipitate was formed due to a chemical reaction between biliverdin and some reagents in the calcium solution. This reaction likely produced a substance that was detected as a strong optoacoustic signal, which was captured by the optoacoustic microscopy after the addition of calcium. The disappearance of the precipitate upon the addition of EGTA supports the idea that calcium ions play a key role in the formation of this reaction product.

Since the $40 \mu L$ calcium solution added during imaging contained $34 \mu L$ HBSS- buffer, $4 \mu L$ $500 \text{ mM } CaCl_2$, and $2 \mu L$ 1.5 mM ionomycin, to further investigate which components were responsible for this precipitation, additional reagents were prepared separately: one solution containing $CaCl_2$ in HBSS- buffer without ionomycin, and another containing

ionomycin in HBSS- buffer without calcium. Two experiments, outlined in Table 5 below, were conducted to clarify the roles of these reagents.

Table 5: Experimental design and results to investigate the formation of black precipitation

	+ ionomycin in HBSS-	+ Ordinary Ca^{2+} solution (ionomycin, Ca^{2+} in HBSS-)	+ Ordinary EGTA solution (ionomycin, EGTA in HBSS-)
Dish with $25 \mu M$ biliverdin	No OA response	Increase in OA signal Form precipitate	Decrease in OA signal Precipitate disappears

	+ Ca^{2+} in HBSS-	+ Ordinary Ca^{2+} solution (ionomycin, Ca^{2+} in HBSS-)	+ Ordinary EGTA solution (ionomycin, EGTA in HBSS-)
Dish with $25 \mu M$ biliverdin	No OA response	Increase in OA signal Form precipitate	Decrease in OA signal Precipitate disappears

From these experiments, it became clear that both calcium ions and ionomycin are necessary to induce the formation of black precipitation when combined with biliverdin. However, in the absence of ionomycin, the initial (original) optoacoustic signal was too weak, resulting in an inadequate calcium response, as no significant signal decrease could be detected following calcium addition. Therefore, further optimization of the GECI biosensor is required to enhance its baseline OA signal, which would allow a proper calcium-dependent optoacoustic response to be captured clearly in future experiments.

3.3 Confocal and optoacoustic imaging in *E. Coli*

Confocal imaging: Calcium reaction

To evaluate the calcium response of GECI sensors in *E. coli*, time-lapse confocal imaging was performed to monitor real-time fluorescence changes following calcium stimulation. Imaging was conducted over a total of 1,100 frames, with each frame captured every 3.72 seconds, resulting in a total acquisition time of approximately 70 minutes. To enhance signal stability and minimize noise, each frame was acquired using the 4 \times frame averaging function in the ZEISS imaging software, where each final image represents the average of four consecutive captures.

In the experimental group, 3 mL of calcium-negative buffer was added to the imaging dish immediately before imaging. While this step is not essential for confocal microscopy, it is required for optoacoustic imaging, as the ultrasound transducer must be immersed in liquid to effectively detect acoustic signals. At frame 30 (roughly 1.86 minutes into the recording), 2 mL of calcium-positive buffer was carefully added to induce a calcium-dependent response. In the control group, the same initial volume of calcium-negative buffer was added before imaging, followed by an additional 2 mL of calcium-negative buffer at the same time point, serving as a negative control to account for mechanical or dilution effects. Representative time-series results for the V8.4 variant are shown below in **Figure 22**.

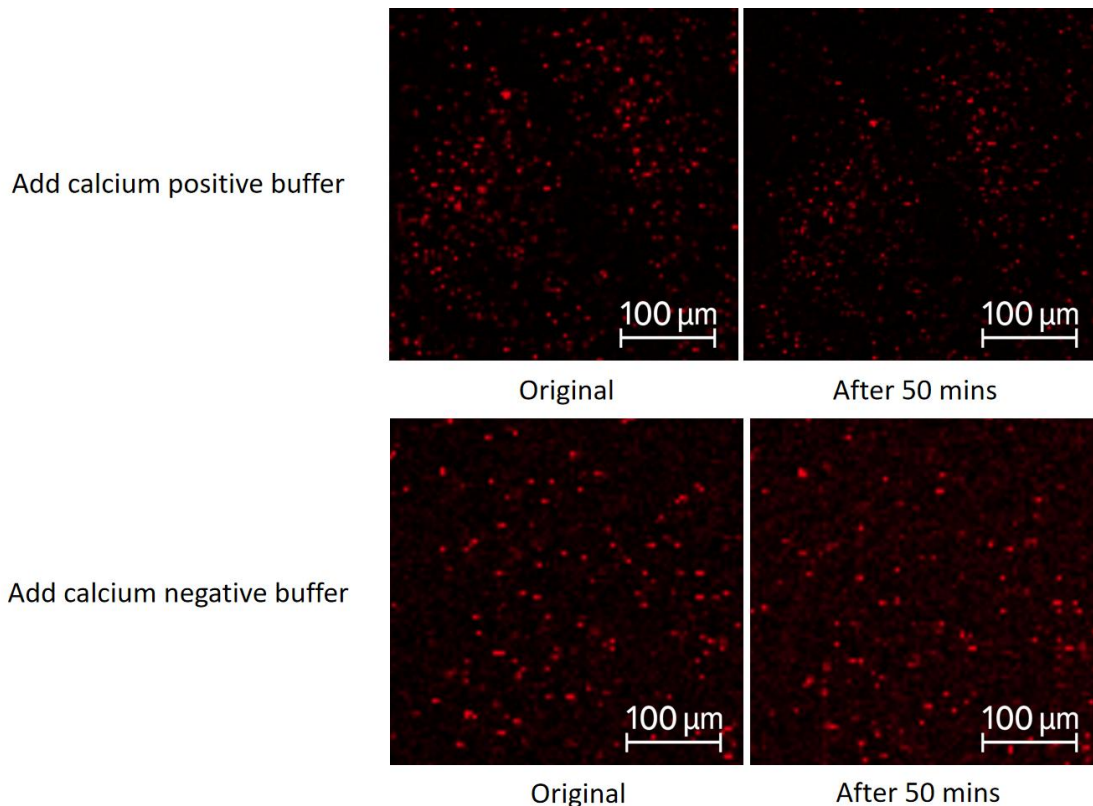


Figure 22: Confocal fluorescence images of *E. coli* colonies expressing V8.4. Top row: Experimental group with 2 mL of calcium-positive buffer added at cycle 30. A decrease in fluorescence intensity is observed 50 minutes post-treatment, indicating sensor response to elevated calcium. Bottom row: Control group with 2 mL of calcium-negative buffer added instead. Fluorescence levels remain relatively stable or slightly increase over the same time period.

As shown in the confocal images above, a visual comparison suggests a decrease in fluorescence intensity 50 minutes after the addition of 2 mL of calcium-positive buffer (top row). Although the fluorescence drop is evident, it appears less pronounced compared to that observed in HEK cells. This diminished response may be attributed to the presence of the agar layer, which likely hindered the diffusion of calcium ions toward the *E. coli* colonies located at the bottom of the dish. In contrast, the fluorescence intensity in the control group (bottom row), where 2 mL of additional calcium-negative buffer was added instead, remained largely unchanged or showed a slight increase after 50 minutes.

To quantitatively assess the fluorescence change during the calcium reaction, the mean fluorescence intensity of both experimental and control groups was analyzed and plotted as a function of time. As shown in **Figure 23**, the fluorescence signal in the experimental group (after addition of calcium-positive buffer) exhibited a gradual decline over the 4,000-second

imaging period, resulting in an overall decrease of approximately 5% relative to the initial baseline. This sustained drop likely reflects the delayed diffusion of calcium ions through the agar layer, suggesting that further fluorescence reduction may occur if additional time is allowed for calcium penetration to reach the bacterial layer.

Add 2 ml 39 μ M calcium-positive buffer

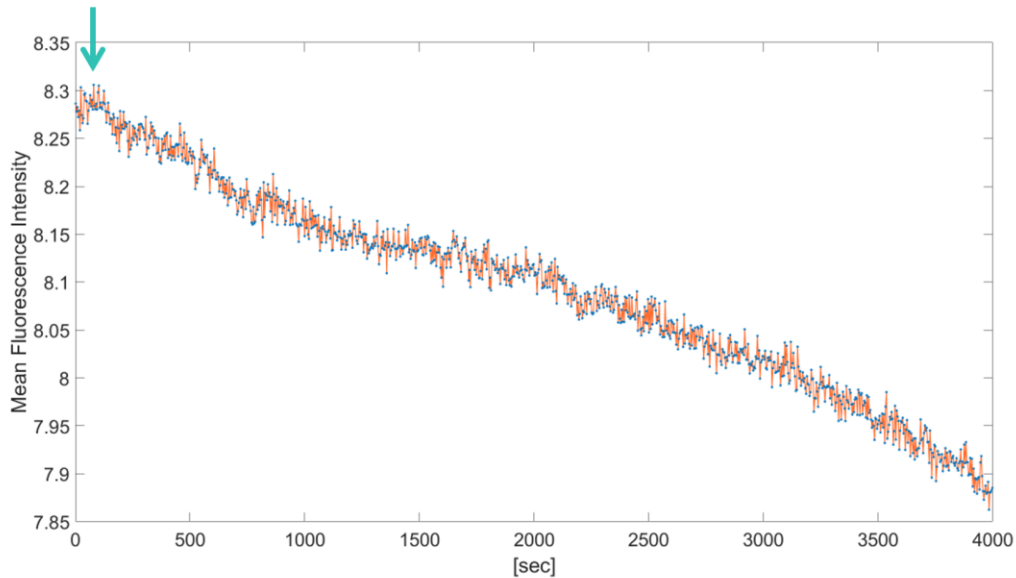


Figure 23: Time-resolved fluorescence intensity of *E. coli* expressing V8.4 following calcium addition. After the addition of 2 mL calcium-positive buffer at the indicated time point, the fluorescence intensity gradually decreased over the 4,000-second recording period, showing an overall drop of approximately 5%. This slow decline likely results from delayed calcium diffusion through the agar layer to the bacterial colonies, suggesting that further signal reduction may occur with prolonged incubation.

The fluorescence change observed in the control group is shown in **Figure 24** below. Over the course of the imaging session, the final mean fluorescence intensity increased by approximately 4%. This rise in signal is likely due to the presence of EGTA in the calcium-negative buffer, which may have diffused into the bacterial cells and chelated intracellular calcium ions. As a result, the intracellular free calcium concentration decreased, leading to a slight increase in fluorescence consistent with the inverse calcium response of the sensor.

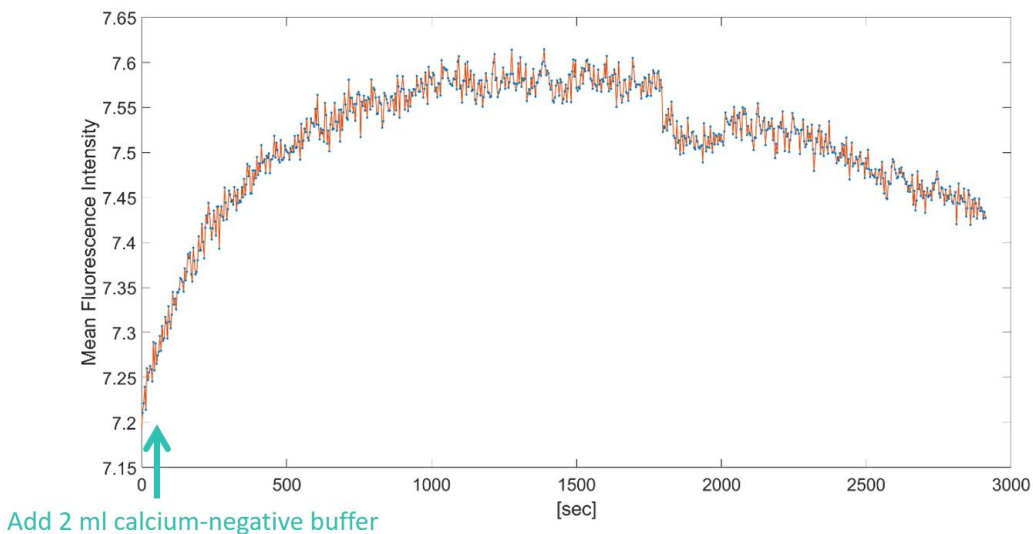


Figure 24: Fluorescence intensity change in the control group after the addition of calcium-negative buffer. The mean fluorescence intensity of *E. coli* colonies expressing V8.4 was monitored over 3,000 seconds after the addition of 2 mL calcium-negative buffer. A gradual increase in fluorescence signal of approximately 4% was observed during the imaging session. This rise is likely attributable to the diffusion of EGTA into the cells, which chelated intracellular calcium ions and thereby lowered cytosolic calcium levels.

Optoacoustic imaging: Calcium reaction

Similar to the confocal imaging setup, optoacoustic imaging was conducted to monitor the calcium response in real time. After the addition of buffer to the imaging dishes, optoacoustic signals were recorded at 30-minute intervals, resulting in a total of four time points: 0, 30, 60, and 90 minutes.

For the experimental group, 5 mL of calcium-positive buffer ($39 \mu\text{M} \text{ Ca}^{2+}$ concentration) was added to the dish immediately prior to the first scan (time = 0 min). In the control group, 5 mL of PBS was used instead of calcium buffer at the same time point. These imaging sessions aimed to determine whether the presence or absence of calcium would lead to measurable changes in optoacoustic signal intensity over time. The resulting OA images of V8.4 for both conditions are shown below in **Figure 25**.

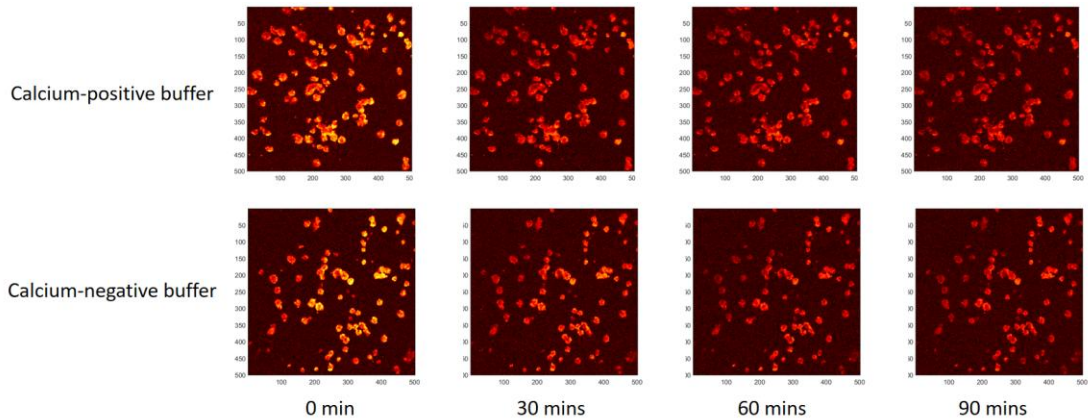


Figure 25: Representative optoacoustic microscopy images of *E. coli* colonies expressing V8.4, acquired at 0, 30, 60, and 90 minutes after buffer addition. In the calcium-positive group (top row), 5 mL of calcium-positive buffer was added immediately before the first imaging. In the calcium-negative control group (bottom row), 5 mL of PBS was added instead. A gradual decrease in signal intensity is observed in both groups. However, it remains unclear whether the observed signal decrease in the calcium-positive group is solely attributable to photobleaching or partially driven by calcium-induced reaction.

As shown above, the optoacoustic signal intensity gradually decreased over time in both the calcium-positive and calcium-negative groups. In the control group (calcium-negative buffer), this decline is likely attributable to photobleaching caused by repeated laser exposure, rather than a true biological response. However, in the calcium-positive group, it remains unclear whether the observed signal reduction is solely due to photobleaching or partially driven by calcium-induced changes. To further investigate this, the optoacoustic signal intensities at all four time points (0, 30, 60, and 90 minutes) were quantified for both groups. The baseline signal (time = 0) was normalized to 1 to facilitate direct comparison, as shown in

Figure 26.

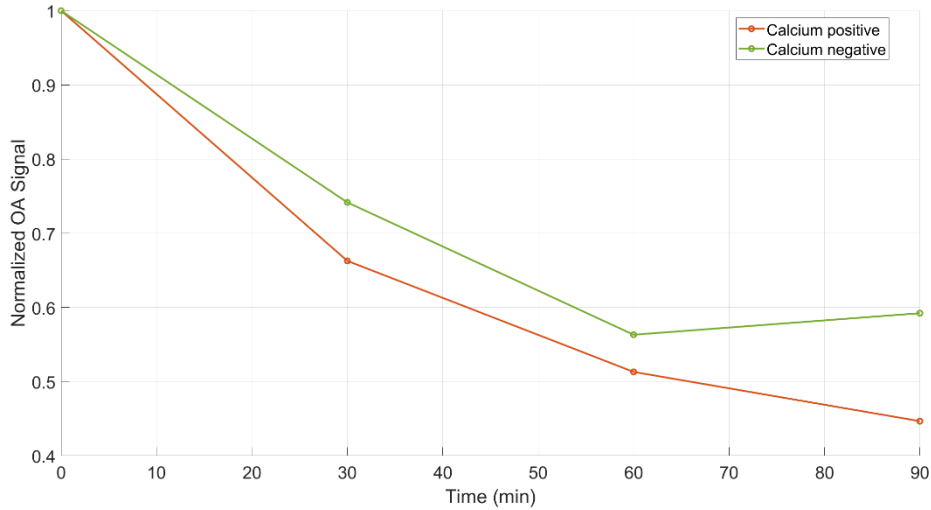


Figure 26: Quantitative comparison of normalized optoacoustic signal intensity over time in calcium-positive and calcium-negative (PBS) groups. While both groups show signal decay, the calcium-positive group exhibits a steeper decline, consistent with calcium-induced optoacoustic signal changes beyond baseline photobleaching.

As shown above, both the calcium-positive and calcium-negative (PBS) groups exhibit a gradual decline in optoacoustic signal over time. However, the calcium-positive group shows a more pronounced and rapid decrease compared to the control, suggesting that the decline is not solely attributable to photobleaching but may also reflect a calcium-induced conformational change in the chromophore. This observation provides further evidence that the sensor is capable of responding to calcium through an optoacoustic mechanism.

3.4 Protein characterization

Visual comparison of absorbance

To compare the absorbance of the four protein variants, all purified proteins were diluted to a concentration of $30 \mu M$ using NaCl/Tris buffer. The degree of light absorption by the protein directly correlates with the intensity of the blue coloration in the protein solution. This comparison is illustrated in **Figure 27** below. From left to right, the protein variants are as follows: NIR-GECO3, V5.2, V6.2, and V8.4. It is clearly observed that NIR-GECO3 exhibits the lightest color, while both V6.2 and V8.4 show more intense blue coloration compared to NIR-GECO3 and V5.2. Also, the difference in intensity between V6.2 and V8.4 is subtle.

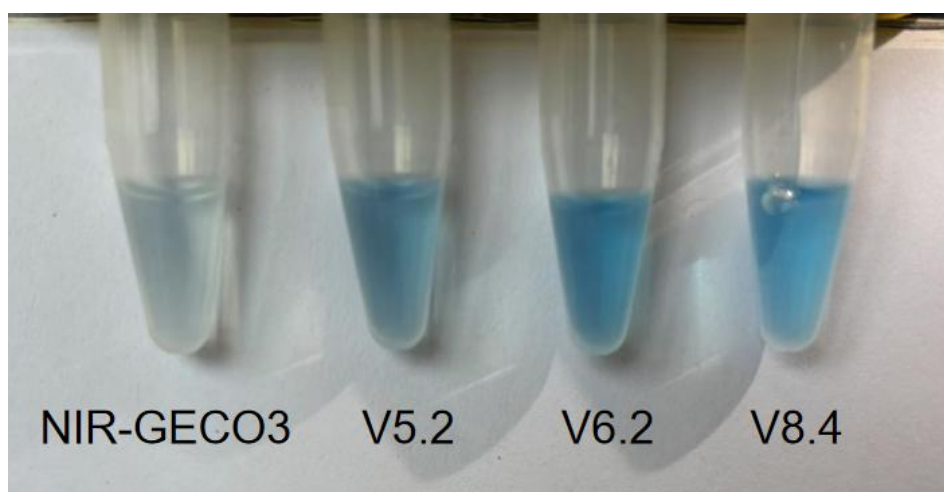


Figure 27: Comparison of different protein variants obtained from directed evolution. All proteins are at the same concentration of $30 \mu M$. From left to right, the protein variants are NIR-GECO3, V5.2, V6.2, and V8.4. The differences in blue intensity observed across the variants reflect the variations in protein absorbance, with V6.2 and V8.4 exhibiting more intense blue coloration compared to NIR-GECO3 and V5.2.

Absorbance spectra

The absorbance spectrum of all four protein variants without calcium is presented in **Figure 28** below. The absorbance is plotted against wavelength, providing a representation of the proteins' light absorption properties across the UV-visible spectrum. From top to bottom, the protein variants are as follows: V8.4, V6.2, V5.2, and NIR-GECO3. Upon examining the figure, it is evident that all four protein variants exhibit a prominent absorbance peak around 650 nm. This indicates that the peak wavelength of absorbance remained consistent through directed evolution, which aligns with the expected outcome. Importantly, the figure also

demonstrates a clear trend: as a result of directed evolution, the overall absorbance of the proteins has increased. The absorbance of V8.4 at around 650 nm is approximately five times higher than that of NIR-GECO3, confirming that the directed evolution process has indeed enhanced the protein's light absorption capacity.

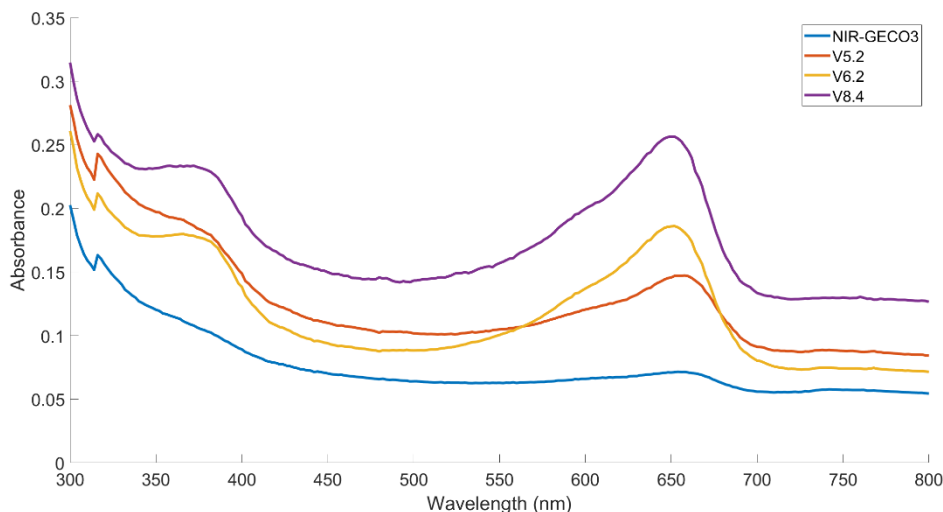


Figure 28: The absorbance spectra of all protein variants from 300 nm to 800 nm. All proteins have an absorbance peak at around 650 nm, and the absorbance increases with directed evolution.

Next, the effect of calcium binding on the absorbance spectrum is shown in **Figure 29**. Delta Absorbance is plotted against wavelength, where Delta Absorbance is calculated by subtracting the absorbance in the presence of $3 \mu M$ calcium from the absorbance in the absence of calcium. This provides a clear indication of the changes in protein absorbance upon calcium binding. As shown in the figure, V8.4 exhibited the largest change in absorbance, followed by V6.2, V5.2, and NIR-GECO3. Notably, the peak absorbance shift occurred around 650 nm for all variants, which is consistent with the trend observed in the absence of calcium. These results demonstrate that V8.4 shows the most significant sensitivity to calcium binding, as reflected in the larger change in absorbance. This enhanced calcium sensitivity suggests that V8.4 is capable of producing a more pronounced change in the output signal, making it a more sensitive calcium sensor compared to the other variants.

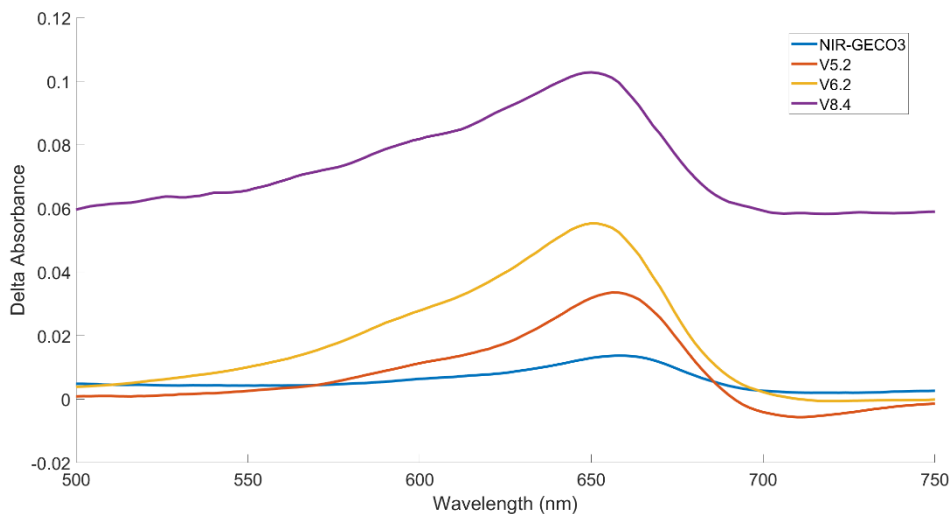


Figure 29: Calcium reaction of all protein variants. Delta Absorbance is calculated by subtracting the absorbance in the presence of $3 \mu M$ calcium from the absorbance in the absence of calcium.

Excitation and emission spectra

Figure 30 displays the normalized excitation and emission spectra of all protein variants in the absence of calcium plotted against wavelength. The dashed curves on the left represent the excitation spectra, while the solid curves on the right indicate the emission spectra. To allow for a clear comparison, the maximum fluorescence of both the excitation and emission spectra of V8.4 was normalized to 1, since V8.4 exhibits the highest fluorescence intensity among the four protein variants. This is followed by V6.2, V5.2, and NIR-GECO3, as anticipated from the sequence of directed evolution. The excitation peak of V8.4 occurs at around 650 nm and the emission peak at approximately 690 nm. These peaks are about 10 times higher in fluorescence intensity compared to NIR-GECO. Interestingly, comparing the absorbance and fluorescence spectra, while the absorbance peak of V8.4 at 650 nm is approximately only 5 times higher than that of NIR-GECO3, the increase in fluorescence intensity is substantially greater. This suggests that, through directed evolution, a larger portion of the increased absorbance is converted into emitted fluorescence rather than ultrasound signals. However, since these proteins are designed to function as calcium sensors based on the optoacoustic effect, there is potential for further optimization. Future improvements could focus on converting a greater fraction of the absorbed light into ultrasound signals, thereby enhancing the protein's performance as an optoacoustic-based calcium sensor.

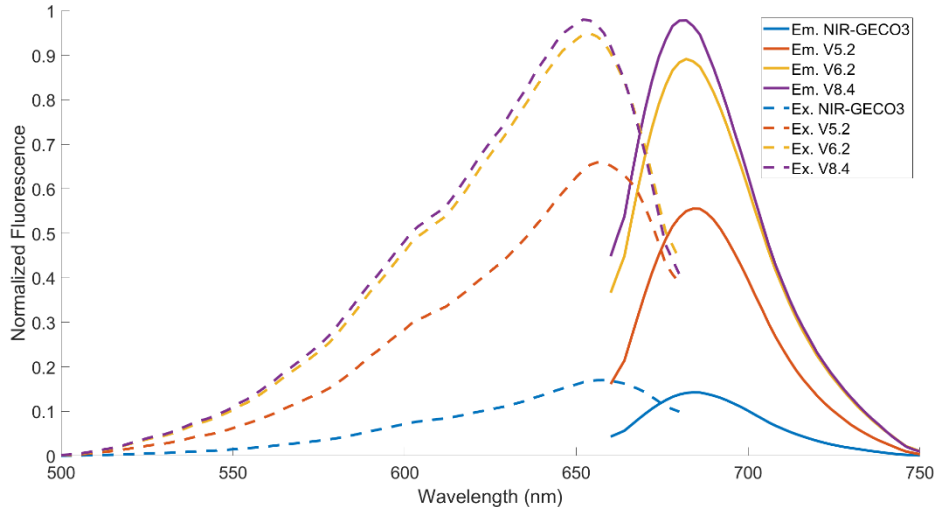


Figure 30: The normalized excitation and emission spectra of all protein variants in the absence of calcium plotted against wavelength. The dashed curves on the left represent the excitation spectra, and the solid curves on the right indicate the emission spectra. The maximum fluorescence of both the excitation and emission spectra of V8.4 was normalized to 1 to allow for comparison.

Next, **Figure 31** presents the calcium reaction of all protein variants, as measured by the change in fluorescence upon calcium binding. The dashed curves on the left represent the changes in excitation spectra, while the solid curves on the right indicate the changes in emission spectra. Similar to the previous analysis of absorbance, Delta Fluorescence is calculated by subtracting the fluorescence signal in the presence of $3 \mu M$ calcium from the fluorescence signal in the absence of calcium. Interestingly, although the change in absorbance was largest for V8.4, followed by V6.2, V5.2, and NIR-GECO3, which aligns with the trends observed in the directed evolution process, the pattern observed in the fluorescence change differs. The largest fluorescence change was observed in V5.2, followed by V6.2, V8.4, and NIR-GECO3, both for the excitation and emission spectra.

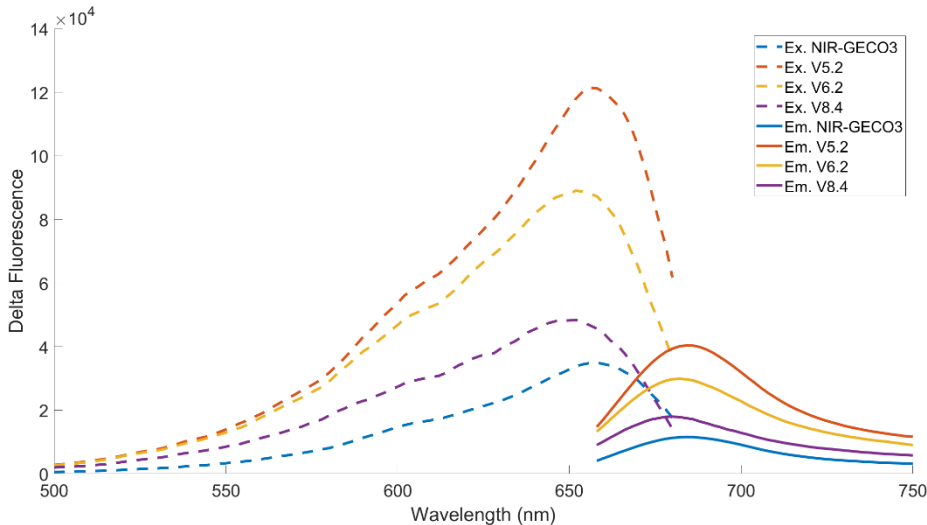


Figure 31: The calcium reaction of all protein variants, as measured by the change in fluorescence upon calcium binding. The dashed curves on the left represent the changes in excitation spectra, and the solid curves on the right indicate the changes in emission spectra. Delta Fluorescence is calculated by subtracting the fluorescence signal in the presence of $3 \mu\text{M}$ calcium from the fluorescence signal in the absence of calcium.

This observation suggests that upon calcium binding, the decrease in absorbance for V6.2 and V8.4 is larger than V5.2, but the majority of this decrease does not come from fluorescence reduction. Instead, a larger fraction of the decrease in absorbance is likely attributed to the reduction in optoacoustic signal, which is consistent with the hypothesis that V6.2 and V8.4 act as a more sensitive calcium probe based on the optoacoustic effect. In contrast, V5.2 exhibit a smaller decrease in absorbance upon calcium binding compared to V6.2 and V8.4. However, this difference is largely attributed to the reduction in fluorescence intensity rather than a significant change in the optoacoustic signal. As a result, V5.2 is considered a less sensitive calcium probe when evaluated in terms of the optoacoustic effect.

Optoacoustic spectra

Figure 32 below shows the optoacoustic spectra of the protein variants measured using optoacoustic tomography in the absence of calcium. As expected, all variants exhibit a peak around 640–650 nm, consistent with their excitation maxima observed in fluorescence measurements. Notably, the OA signal amplitude increases progressively from V5.2 to V6.2 to V8.4, which aligns with the order of directed evolution. This trend confirms the effectiveness of the evolutionary process in enhancing optoacoustic signal strength.

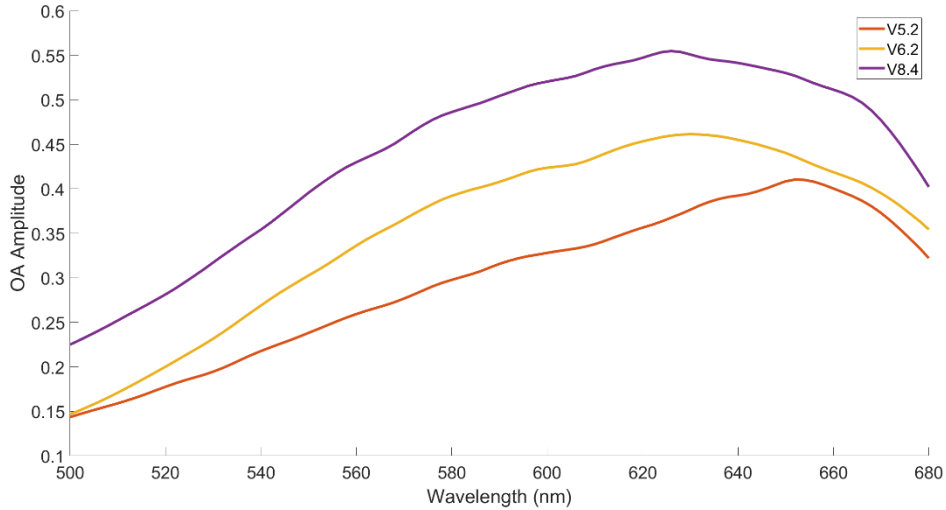


Figure 32: Optoacoustic spectra of GECI variants V5.2, V6.2, and V8.4 measured in the absence of calcium. From bottom to top, the OA signal amplitude increases in the order of V5.2, V6.2, and V8.4, consistent with the progression of directed evolution. All three variants display a spectral peak around 640–650 nm, matching their known fluorescence excitation maxima.

Figure 33 illustrates the individual calcium responses of protein variants V5.2, V6.2, and V8.4, measured through their optoacoustic spectra in both calcium-negative (solid line) and calcium-positive (dashed line) conditions. For both V6.2 and V8.4, the expected trend is observed: the optoacoustic signal is stronger in the absence of calcium and decreases upon the addition of $39 \mu M Ca^{2+}$, consistent with the known inverse correlation between calcium concentration and fluorescence intensity for GECIs of the NIR-GECO family. Also, the absolute change in the optoacoustic signal is similar for V8.4 and V6.2.

However, an anomalous behavior is observed for V5.2. While both calcium-positive and calcium-negative curves peak around 650 nm, the calcium-positive signal exceeds the calcium-negative one in that region. This is contrary to the expected signal suppression upon calcium binding. Notably, in **Figure 31**, which shows the calcium-induced change in fluorescence intensity, V5.2 exhibits the largest fluorescence decrease among the three variants upon calcium binding. In contrast, in **Figure 33**, its optoacoustic signal decreases only marginally, and at the peak, it paradoxically increases.

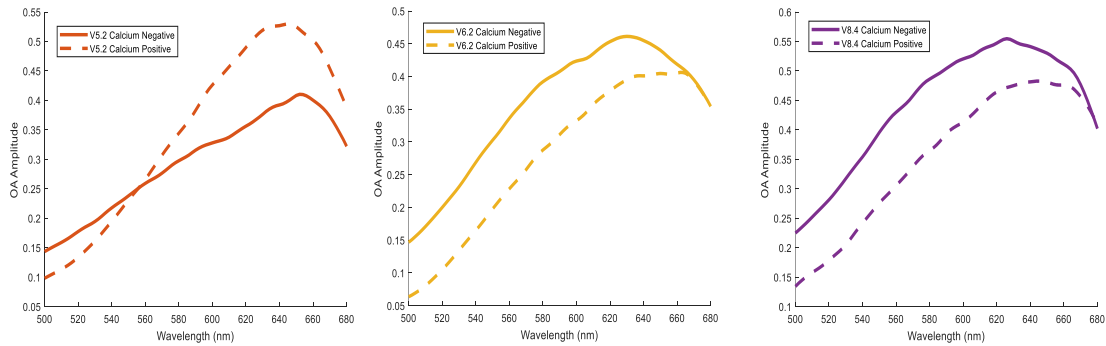


Figure 33: Optoacoustic spectral response of protein variants V5.2, V6.2, and V8.4 under calcium-negative and calcium-positive conditions. Solid lines represent calcium-negative conditions, while dashed lines represent calcium-positive conditions ($39 \mu M Ca^{2+}$). V6.2 and V8.4 exhibit the expected calcium response, with OA signal decreases upon calcium binding. In contrast, V5.2 shows an abnormal pattern, with the calcium-positive signal exceeding the calcium-negative signal around its peak wavelength (~ 650 nm).

This discrepancy can be understood in the context of light energy distribution. The absorbed light energy (measured by absorbance) is partitioned into fluorescence emission and heat-induced pressure waves (measured as optoacoustic signal). Thus, a decrease in total absorbance upon calcium binding for V5.2 is accompanied by a disproportionate drop in fluorescence emission, leaving a relatively higher fraction of absorbed energy to be converted into ultrasound. This redistribution could explain the slight increase in optoacoustic signal at peak wavelengths.

To explain this inconsistency, plasmid sequencing was performed for all four protein variants (NIR-GECO3, V5.2, V6.2, and V8.4). Sequencing revealed that only the plasmid labeled as V5.2 contained abnormalities, including point mutations, deletions, and mismatches in the promoter region as well as three codon-level deviations in the coding region itself. These alterations were not present in the correctly sequenced plasmids of NIR-GECO3, V6.2, and V8.4. It is therefore likely that the current V5.2 construct is not the genuine product of round 5, variant 2 of the directed evolution workflow. This could account for its abnormal calcium response and deviation from the expected optoacoustic and fluorescence behavior.

Chapter 4: Conclusion

This thesis presents a comprehensive evaluation of three optoacoustic-based genetically encoded calcium indicators (V5.2, V6.2, and V8.4) developed through eight rounds of directed evolution from the parental NIR-GECO3 protein. These variants were designed with the aim of enhancing optical absorbance, optoacoustic signal strength, photostability, and dynamic responsiveness to calcium. By integrating confocal fluorescence microscopy, optoacoustic imaging, and *in vitro* protein characterization, we explored their functional performance in both mammalian and bacterial systems.

Our findings demonstrate that while directed evolution has already led to significant improvements in overall signal strength and spectral properties, the results also indicate that these proteins retain substantial room for further optimization. In particular, V8.4 consistently outperformed V5.2 and V6.2 in multiple dimensions: it exhibited the highest baseline optoacoustic amplitude and the strongest calcium-induced change, thereby offering the most sensitive and reliable response for optoacoustic-based calcium sensing. Moreover, experiments performed in *E. coli* confirmed that calcium-induced optoacoustic responses could be captured in a prokaryotic context.

In conclusion, the project confirms the feasibility of using GECIs as dynamic optoacoustic sensors for calcium imaging and establishes a strong methodological foundation for developing future GECIs with optoacoustic calcium sensitivity. Continued efforts in protein optimization and experimental standardization are essential for translating these biosensors into viable tools for deep-tissue and long-term *in vivo* neuroimaging.

References

1. Choquet, D., M. Sainlos, and J.B. Sibarita, *Advanced imaging and labelling methods to decipher brain cell organization and function*. Nature Reviews Neuroscience, 2021. **22**(4): p. 237-255.
2. Gross, J., et al., *Dynamic imaging of coherent sources:: Studying neural interactions in the human brain*. Proceedings of the National Academy of Sciences of the United States of America, 2001. **98**(2): p. 694-699.
3. Xie, L.J., et al., *PET brain imaging in neurological disorders*. Physics of Life Reviews, 2024. **49**: p. 100-111.
4. Backskai, B.J., et al., *Imaging of amyloid- β deposits in brains of living mice permits direct observation of clearance of plaques with immunotherapy*. Nature Medicine, 2001. **7**(3): p. 369-372.
5. Keu, K.V., et al., *Reporter gene imaging of targeted T cell immunotherapy in recurrent glioma*. Science Translational Medicine, 2017. **9**(373).
6. Min, B.K., M.J. Marzelli, and S.S. Yoo, *Neuroimaging-based approaches in the brain-computer interface*. Trends in Biotechnology, 2010. **28**(11): p. 552-560.
7. Klohs, J. and M. Rudin, *Unveiling Molecular Events in the Brain by Noninvasive Imaging*. Neuroscientist, 2011. **17**(5): p. 539-559.
8. Razansky, D., J. Klohs, and R.Q. Ni, *Multi-scale optoacoustic molecular imaging of brain diseases*. European Journal of Nuclear Medicine and Molecular Imaging, 2021. **48**(13): p. 4152-4170.
9. Qian, Y., et al., *A genetically encoded near-infrared fluorescent calcium ion indicator*. Nature Methods, 2019. **16**(2): p. 171-+.
10. Dana, H., et al., *High-performance calcium sensors for imaging activity in neuronal populations and microcompartments*. Nature Methods, 2019. **16**(7): p. 649-+.

11. Nakai, J., M. Ohkura, and K. Imoto, *A high signal-to-noise Ca(2+) probe composed of a single green fluorescent protein*. Nat Biotechnol, 2001. **19**(2): p. 137-41.
12. Tian, L., et al., *Imaging neural activity in worms, flies and mice with improved GCaMP calcium indicators*. Nature Methods, 2009. **6**(12): p. 875-U113.
13. Akerboom, J., et al., *Genetically encoded calcium indicators for multi-color neural activity imaging and combination with optogenetics*. Frontiers in Molecular Neuroscience, 2013. **6**.
14. Dana, H., et al., *Sensitive red protein calcium indicators for imaging neural activity*. Elife, 2016. **5**.
15. Qian, Y., et al., *Improved genetically encoded near-infrared fluorescent calcium ion indicators for in vivo imaging*. PLoS Biol, 2020. **18**(11): p. e3000965.
16. Ollinger, R., et al., *Therapeutic applications of bilirubin and biliverdin in transplantation*. Antioxid Redox Signal, 2007. **9**(12): p. 2175-85.
17. Brunker, J., et al., *Photoacoustic imaging using genetically encoded reporters: a review*. J Biomed Opt, 2017. **22**(7).
18. Ikeno, T., et al., *Design and Synthesis of an Activatable Photoacoustic Probe for Hypochlorous Acid*. Analytical Chemistry, 2019. **91**(14): p. 9086-9092.
19. Hu, S., K. Maslov, and L.V. Wang, *Second-generation optical-resolution photoacoustic microscopy with improved sensitivity and speed*. Optics Letters, 2011. **36**(7): p. 1134-1136.
20. Yang, H., et al., *Soft ultrasound priors in optoacoustic reconstruction: Improving clinical vascular imaging*. Photoacoustics, 2020. **19**.
21. Zhang, J., et al., *Resolution Enhancement Strategies in Photoacoustic Microscopy: A Comprehensive Review*. Micromachines (Basel), 2024. **15**(12).
22. Wang, L.V. and S. Hu, *Photoacoustic tomography: in vivo imaging from organelles to organs*. Science, 2012. **335**(6075): p. 1458-62.
23. Dean-Ben, X.L. and D. Razansky, *Functional optoacoustic human angiography with handheld video rate three dimensional scanner*. Photoacoustics, 2013. **1**(3-4): p. 68-73.

24. Gottschalk, S., et al., *Rapid volumetric optoacoustic imaging of neural dynamics across the mouse brain*. Nature Biomedical Engineering, 2019. **3**(5): p. 392-401.
25. Deán-Ben, X.L., et al., *Advanced optoacoustic methods for multiscale imaging of dynamics*. Chemical Society Reviews, 2017. **46**(8): p. 2158-2198.
26. Deán-Ben, X.L., et al., *Functional optoacoustic neuro-tomography for scalable whole-brain monitoring of calcium indicators*. Light-Science & Applications, 2016. **5**.
27. Filonov, G.S., et al., *Deep-Tissue Photoacoustic Tomography of a Genetically Encoded Near-Infrared Fluorescent Probe*. Angewandte Chemie-International Edition, 2012. **51**(6): p. 1448-1451.
28. Li, Y., et al., *Engineering Dark Chromoprotein Reporters for Photoacoustic Microscopy and FRET Imaging*. Sci Rep, 2016. **6**: p. 22129.
29. Holehonnur, R., et al., *The production of viral vectors designed to express large and difficult to express transgenes within neurons*. Mol Brain, 2015. **8**: p. 12.

Acknowledgements

First and foremost, I would like to express my deepest gratitude to my supervisor, Prof. Dr. Daniel Razansky, for giving me the opportunity to join his research group and contribute to this exciting project. His invaluable guidance, continuous encouragement, and unwavering support throughout the course of my Master's thesis have been instrumental to both my academic development and the completion of this work. I am equally grateful to my co-supervisor, Dr. Xiang Liu, for his patient mentorship, technical advice, and generous help in experimental design, data analysis, report revision, and so much more. His consistent support and critical suggestions greatly enriched the quality of my work and my learning experience. I would also like to thank all the members of the lab for providing a friendly and collaborative research environment. My sincere thanks also go to Miho Sato, who supported me so much during the first three months of this thesis. She patiently taught me so many things, both experimental skills and theoretical knowledge, and never hesitated to help, no matter how many questions I asked. I am also truly grateful for her kindness in teaching me Japanese and for sharing with me the beauty of everyday life in Japan. Her support meant a lot to me, both inside and outside the lab.

Over the past two years, I could not have completed my Master's journey in Zurich without the unwavering love, support, and encouragement from my family. First, my heartfelt thanks go to my parents. Thank you for always standing behind me, no matter how far I chose to go or how uncertain the road ahead seemed. Your quiet strength and constant encouragement have been the anchor of my life, giving me the freedom to dream boldly and walk my own path. I would also like to express my gratitude to my cousin. Thank you for always being there and growing up with me. Thank you for helping me break free from the mental cages that I once thought unshakable, for trusting me when I was overwhelmed by self-doubt and hesitation, for offering me a sense of safety and comfort when I felt helpless and insecure, and for sharing all the tears and laughter while we were watching *One Piece*!

I would also like to say thank you to my friends. You have given me so much support, warmth, and energy during the journey, which made me feel I am truly lucky and blessed from the bottom of my heart.

To Yinglin, thank you for always standing by my side since high school. I am especially grateful for your trust and companionship during my darkest days back then. I will always cherish the memories we shared in Hangzhou, like the birthday cake at Starbucks, the Polaroid you took and decorated for me, and the dinner by the West Lake after a full day of walking. Thank you, too, for the birthday drawing, which is one of the most precious gifts I have ever received. I will always remember all the encouragement and care you have given me along the way, and I look forward to sharing many more memories together.

To Xenowei, thank you for your companionship, also ever since high school! I will always cherish the memory of us walking through Huangzhong Park near my home in Chengdu, sharing what felt like endless and also meaningless conversations. Thank you for sharing your beautiful travel moments with me and they made me feel like I was part of your journey, too. Thank you for all the thoughtful birthday gifts, and for keeping our tradition of exchanging presents since we were both born in August. I truly hope, and firmly believe, that your upcoming Master's journey will be both happy and meaningful! I cannot wait to see all the wonderful things you will experience and achieve.

To Wenwen, I remember when I met you during the final training at Sichuan University. Even though we had only known each other for a few days back then, I already felt an instant connection with you, as if you were an old friend with whom I could be completely at ease. It was a rare and precious feeling I had never experienced before, and ever since, you have been a truly cherished friend in my life. Thank you for sharing our bizarre dreams with each other, for keeping me company with those seemingly meaningless phone calls just because I miss my hometown dialect, for singing to me on the phone when I was scared walking alone at night, and for so many other little things and words that have meant the world to me.

To Yihan, you are the one who made my memories at UIUC so special whenever I think back on my time in the U.S.. Thank you for playing *guqin* for me, and for your beautiful

drawings. I think you are truly a gifted artist. Thank you for listening to my piano playing and always finding something good to say so sincerely, no matter how terrible I thought I had played. I am also grateful for all the dinners you made for me, and for the Jia Zhangke films we watched together late into the night. Thank you for all the wonderful recommendations on introductions to Chinese literature, culture, and beyond. They have inspired me and deepened my appreciation for our heritage. Thank you for spending time with me when I traveled to Sweden that Christmas two years ago. I hope you'll always stay happy, confident, and full of love for life and the people around you.

To Leleju, I have learned so much from you, even though we have only met a few times. Your opinions are always inspiring, honest, and insightful. Thank you for pointing out my mistakes and helping me reflect on my situations, whether in Cantonese, piano, or life. I truly admire your creativity, with endless ideas flowing from your mind every day. Thank you for always encouraging me to pursue my passions, and for the thoughtful Christmas gift, the drawing of the footprints of my life. I will always keep it close and treasure the meaning it carries with me.

To Bretonia's haixiuyouling, I feel so lucky to have met you from the very first day I moved into this dormitory. Thank you for your patience in teaching me Cantonese, even though I could never quite get the pronunciation right. Thank you for introducing me to frisbee and badminton, though I am such a beginner in badminton and was never able to throw the disc far enough away. These games have filled my life with so much joy, laughter, and energy. Thank you for inviting me to play Switch games. Those moments became the highlights of my weekends and something I always looked forward to. Thank you also for teaching me to draw and for sharing your drawings with me. Your drawings always make me wonder what the world looks like through your eyes. There are far too many things to mention, like the music scores you printed for me, the cherries you shared, all the casual chats in the dorm, and countless other moments that I will always treasure. Most of all, thank you for all the warmth, support, understanding, and encouragement you have given me along my way. May you always remain

happy, brave, and unafraid to journey on, and you will always have my unconditional support, trust, and the warmest wishes from afar.

There are so many others I should also thank. To Yarong, thank you for your patient guidance and constant encouragement in piano and music. Through your teaching, music has become not only a faithful companion in my life, but also a window opening onto a more beautiful and profound world. To Tianchen, thank you for the postcard you sent from Alaska. I feel so grateful to have met you in the piano room back at UIUC, and I wish you continued happiness and strength. To Gyx, thank you for teaching me guitar, and to Lh, thank you for teaching me tennis. I truly cannot imagine a world without all of you.

Lastly, my gratitude goes to my beloved puppy, Duo Duo. Thank you for your sixteen years of companionship, from the very beginning of my memory until two months after I went abroad at the age of twenty. You were there through all the seasons of my childhood and teenage years, quietly offering comfort, joy, and unconditional love. I will always remember you, love you, and carry your pawprints in my heart.

May you run free and stay forever happy and young in the other world.

Declaration of originality

The signed declaration of originality is a component of every written paper or thesis authored during the course of studies. **In consultation with the supervisor**, one of the following two options must be selected:

- I hereby declare that I authored the work in question independently, i.e. that no one helped me to author it. Suggestions from the supervisor regarding language and content are excepted. I used no generative artificial intelligence technologies¹.
- I hereby declare that I authored the work in question independently. In doing so I only used the authorised aids, which included suggestions from the supervisor regarding language and content and generative artificial intelligence technologies. The use of the latter and the respective source declarations proceeded in consultation with the supervisor.

Title of paper or thesis:

Optoacoustic-based GECI Biosensor: An Imaging and Characterization Study

Authored by:

If the work was compiled in a group, the names of all authors are required.

Last name(s):

Chen

First name(s):

Xiyan

With my signature I confirm the following:

- I have adhered to the rules set out in the [Citation Guidelines](#).
- I have documented all methods, data and processes truthfully and fully.
- I have mentioned all persons who were significant facilitators of the work.

I am aware that the work may be screened electronically for originality.

Place, date

Zurich, 25.08.2025

Signature(s)

Xiyan Chen

If the work was compiled in a group, the names of all authors are required. Through their signatures they vouch jointly for the entire content of the written work.

¹ For further information please consult the ETH Zurich websites, e.g. <https://ethz.ch/en/the-eth-zurich/education/ai-in-education.html> and <https://library.ethz.ch/en/researching-and-publishing/scientific-writing-at-eth-zurich.html> (subject to change).